Journal of
ENERGY TECHNOLOGY

Journal of
ENERGY TECHNOLOGY

JET

JOURNAL OF ENERGY TECHNOLOGY

Spoštovani bralci revije Journal of energy technology (JET)

Ekološki vplivi in zmanjšanje zalog fosilnih goriv v svetu sili države v izrabo obnovljivih virov in uporabo alternativnih tehnologij za izrabo virov energije. Zato sta se v EU sprožila pobuda in gibanje, imenovana Evropski zeleni dogovor, ki je bil odobren leta 2020. Evropski zeleni dogovor je sklop političnih pobud Evropske komisije za prehod gospodarstva EU na trajnostni gospodarski model. Najpomembnejši cilj zelenega dogovora je, da Evropska unija do leta 2050 postane podnebno nevtralna.

Poglavitni del zelenega prehoda je uvedba obnovljivih virov energije, tako električne, toplotne kakor tudi energije hladu.

V svetu je veliko držav naredilo že izjemno velik preboj na področju energetike. Naštejmo nekatere najuspešnejše.

- Islandija po podatkih uporablja že več kot 86 % vse energije iz obnovljivih virov. Največji delež predstavlja uporaba geotermalne energije kakor tudi vodne energije.

- Norveška uporablja že več kot 71 % vse energije iz obnovljivih virov, v prihodnjih letih pa načrtujejo še znatno redukcijo izpustov toplogrednih plinov. Zelo dobre rezultate dosegajo tudi Švedska, Brazilija, Nova Zelandija … V absolutnem smislu in v raziskovalnem smislu sta veliko dosegli tudi Kitajska in ZDA.

Tudi v Sloveniji se trudimo doseči zaveze EU pri uporabi obnovljivih virov, trenuten delež obnovljivih virov v energiji znaša približno tretjino. Seveda pa nas čaka še kar nekaj izzivov na področju energetike. Najboljši odgovor na zapleteno energetsko situacijo so nadaljnje raziskave na tem področju. Upajmo, da vsaj nekaj odgovorov lahko najdemo v člankih revije JET. Želim vam zanimivo branje.

Jurij AVSEC
odgovorni urednik revije JET

Dear Readers of the Journal of Energy Technology (JET)

Ecological impacts and the reduction of fossil fuel reserves in the world force countries to use renewable resources and use alternative technologies for the use of energy sources. Therefore, an initiative and movement called the European Green Deal was launched in the EU, which was approved in 2020. The European Green Deal is a set of political initiatives of the European Commission for the transition of the EU economy to a sustainable economic model. The most important goal of the Green Deal is for the European Union to become climate neutral by 2050.

The main part of the green transition is the introduction of renewable energy sources, both electricity, heat and cooling energy.

In the world, many countries have already made an extremely large breakthrough in the field of Energy. Let's list some of the most successful ones.

• According to data, Iceland already uses more than 86% of all energy from renovations. The largest share is represented by the use of geothermal energy, as well as water energy.

• Norway already uses more than 71% of all energy from renewable sources, and, in the coming years, they plan to reduce greenhouse gas emissions significantly. Sweden, Brazil and New Zealand have also achieved very good results. In absolute terms and in terms of research, China and the USA have also achieved a lot.

In Slovenia, too, we are trying to achieve the EU commitments in the use of renewable sources, and the current share of renewable sources in energy amounts to about a third. Of course, there are still quite a few challenges in the field of Energy waiting for us in Slovenia. The best answer to the complex energy situation is further research in this field. Hopefully, at least some answers can be found in the present articles of the JET magazine. I wish you an interesting reading of the current issue of JET magazine.

Jurij AVSEC
Editor-in-chief of JET

Table of Contents
Kazalo

Journal of Energy Technology

INFRARED THERMOGRAPHY IN THE DETECTION OF WATER STRESS IN PLANTS

INFRARDEČA TERMOGRAFIJA PRI ODKRIVANJU VODNEGA STRESA V RASTLINAH

Hrvoje Glavaš [1ℜ] , **Monika Marković** [2], **Antonija Strilić** [2]

Keywords: thermography, water stress, plant, UHI, electrical energy

Abstract

Plants and green islands in urban areas are one way to mitigate climate change and reduce the energy demand for air conditioning. Like humans, plants are also exposed to the urban heat island effect, which manifests itself in the fact that air temperatures in urban areas are on average 2-5°C higher than in rural areas. In addition, plants are exposed to water stress, which occurs when the amount of available water exceeds or falls short of the plants' water requirements. The paper presents an increase in electricity demand, with a special focus on Croatia, Slovenia and countries with similar electricity consumption. The effects of the urban heat island are illustrated using a graphical comparison from the recent literature. Infrared thermography, as one of the methods for detecting water stress, is explained with the physical background of long-wave radiation detection, and compared with near infrared digital photography. All possible aspects are presented of radiation detection that occur during thermographic analysis. A specific overview of water stress is given, and its effects are illustrated using examples of plant height and flower size. The application of infrared thermography in the detection of water stress is illustrated using thermograms of wheat in a dry field and after irrigation. On the basis of the presented information, a conclusion was drawn about the possibility of using infrared thermography in the detection of water stress.

ℜ   Corresponding author: Prof.Dr.Sc. Hrvoje Glavaš, Josip Juraj Strossmayer University of Osijek, Faculty of Electrical Engineering, Computer Science and Information Technology Osijek, Kneza Trpimira 2b, 31000 Osijek, Croatia, Tel.: +38531224600, E-mail address: hrvoje.glavas@ferit.hr

1   Josip Juraj Strossmayer University of Osijek, Faculty of Electrical Engineering, Computer Science and Information Technology Osijek, Kneza Trpimira 2b, 31000 Osijek, Croatia

2   Josip Juraj Strossmayer University of Osijek, Faculty of Agrobiotechnical Sciences Osijek, Vladimira Preloga 1, 31000, Osijek, Croatia

Povzetek

Rastline in zeleni otoki v urbanih območjih so eden od načinov za ublažitev podnebnih sprememb in zmanjšanje povpraševanja po energiji za klimatske naprave. Tako kot ljudje so tudi rastline izpostavljene učinku mestnega toplotnega otoka, ki se kaže v tem, da so temperature zraka v urbanih območjih v povprečju za 2–5 °C višje kot na podeželju. Poleg tega so rastline izpostavljene vodnemu stresu, ki nastane, ko količina razpoložljive vode presega ali pade pod potrebe rastlin po vodi. Prispevek prikazuje porast povpraševanja po električni energiji s posebnim poudarkom na Hrvaški, Sloveniji in državah s podobno porabo električne energije. Učinki mestnega toplotnega otoka so prikazani z grafično primerjavo iz novejše literature. Infrardeča termografija kot ena od metod za zaznavanje vodnega stresa je pojasnjena s fizikalnim ozadjem zaznavanja dolgovalovnega sevanja in primerjana z digitalno fotografijo blizu infrardečega sevanja. Predstavljeni so vsi možni vidiki detekcije sevanja, ki nastanejo pri termografski analizi. Podan je poseben pregled pomanjkanja vode, njegovi učinki pa so prikazani na primerih višine rastline in velikosti cvetov. Uporaba infrardeče termografije pri zaznavanju pomanjkanja vode je prikazana s termogrami pšenice na suhem polju in po namakanju. Na podlagi predstavljenega so sklepali o možnostih uporabe infrardeče termografije pri detekciji vodnega stresa.

1   INTRODUCTION

Since the 1990s climate change has had a negative impact, which is particularly evident in agriculture and the electricity supply. The need for space cooling is increasing. For example, from July 1, 2023, certain types of air conditioning systems in South Australia may only be installed or connected to the electricity distribution network if they meet demand-side management requirements [1]. The International Energy Agency (IEA) stipulates that air conditioning systems installed after July 1, 2053 must be equipped with a demand response system, i.e., they must be controlled via the electricity distribution grid, [2]. All this points to the important role that the availability of split air conditioning systems plays for the electricity system. The development of electricity consumption is best illustrated in Figure 1, data source the International Energy Agency (IEA) [3]
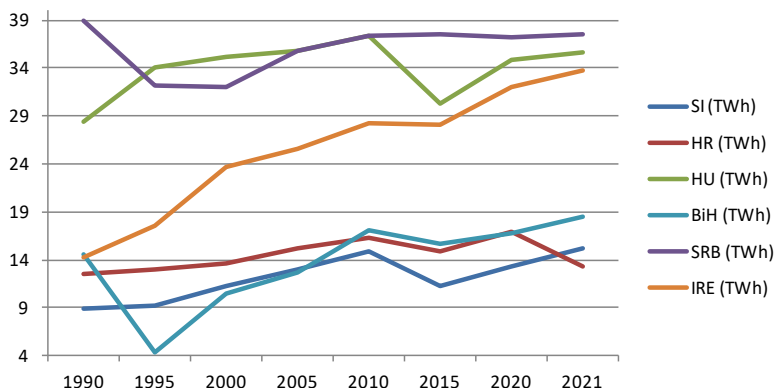
Figure 1: *Electricity consumption in Croatia and Slovenia in TWh compared to arbitrarily selected countries*

Urban centres exposed to solar radiation are built from construction materials with high specific heat capacity, and roads are dark in colour, which makes it easy to absorb and store heat energy. Irradiated energy is released in the form of long-wave radiation, and, since the energy radiating into neighbouring buildings is absorbed and re-emitted into the local environment, it results in warming known as an Urban Heat Island (UHI), [4] The UHI effect manifests itself in the way that air temperatures in urban areas are, on average, 2-5°C higher (in some cases even more than 12°C) compared to rural areas. The spatial trends of the temperature differences can be seen in Figure 2. Each dot represents the temperature difference in a specific city. The mean temperature differences for each country are indicated by the stacked bars.
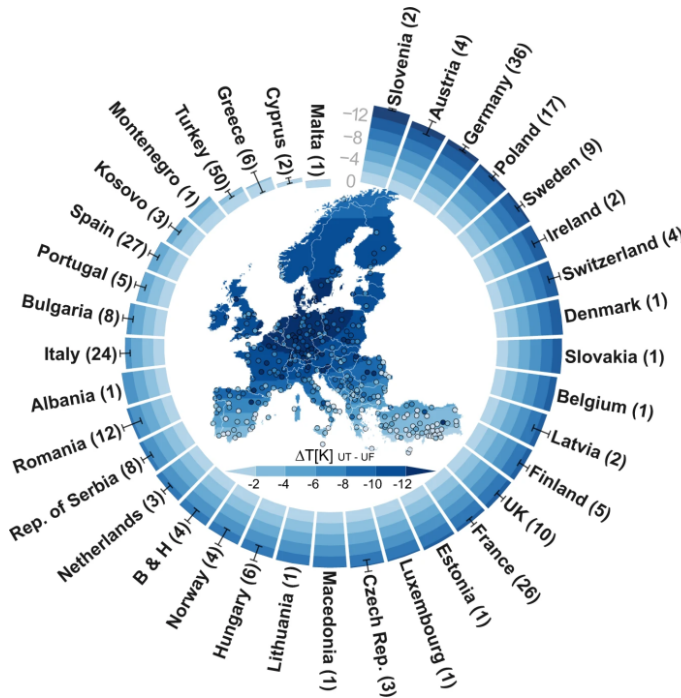
Figure 2: Spatial trends of the temperature differences during hot extremes between areas covered by trees and urban areas, source [6]

The rise in temperature in urban areas leads to considerable ecological and social consequences [5]. A study by the Joint Research Center from May 2023 predicts that more vegetation in certain urban areas can mitigate the extreme heat [7]. More and more attention is being paid to vegetation in the reconstruction of urban areas. The last reconstruction of the Tvrđa Fortress in Osijek [8] resulted in the formation of green islands on the main square, as can be seen in Figure 3. The thermogram shows that the temperature of the trees is 33.8°C and that of the ground is 34.7°C, much lower than the surrounding area at 53.2°C. The lower temperatures are the result of water evaporation. The secondary contribution of the trees is that the area under the canopy reduces the energy radiated by the sun onto the paved area, and the energy is accumulated in materials with a high heat capacity.
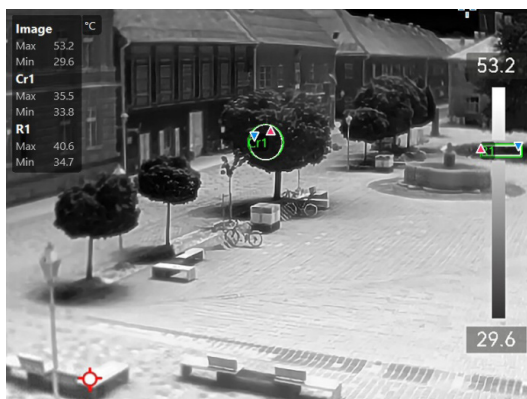
Figure 3: Thermogram of the newly formed green islands of Osjecka Tvrdja

2   INFRARED THERMOGRAPHY AS A METHOD DETECTION OF THERMAL RADIATION

Infrared thermography is a method for detecting thermal radiation (usually in the long-wave range), which is converted into a visible image. Based on a calibration and precisely selected physical parameters that affect the radiation, the corresponding temperature value is related to the amount of radiation. In terms of resolution, which reaches 2560 x 2048, infrared thermography is at the same stage of development as digital photography was more than twenty years ago. This is important to know, because, 10 years ago, there was a major shift in the spread of thermal imaging cameras to the wider market with the emergence of small manufacturers. The similarity ends there, because, unlike photography, which detects light and requires light for excitation, thermography detects radiation, which is a consequence of the internal energy of the observed object, Figure 4.
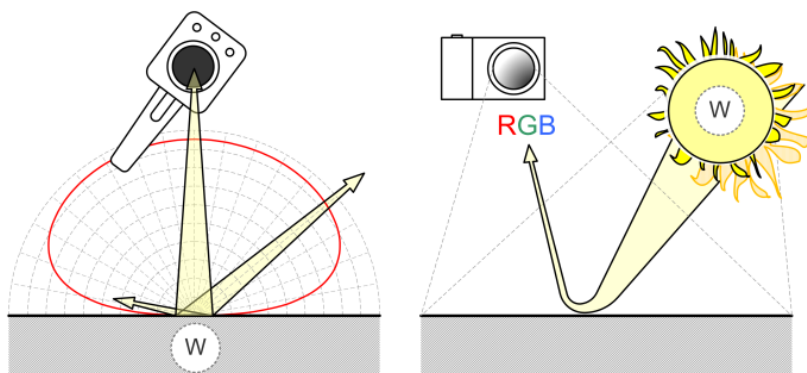
Figure 4: The basic difference between photography and thermography, source [9]

Urban centres exposed to solar radiation are built from construction materials with high specific heat capacity, and roads are dark in colour, which makes it easy to absorb and store heat energy. Irradiated energy is released in the form of long-wave radiation, and, since the energy radiating into neighbouring buildings is absorbed and re-emitted into the local environment, it results in warming known as a Urban Heat Island (UHI), [4] The UHI effect manifests itself in the way that air temperatures in urban areas are, on average, 2-5°C higher (in some cases even more than 12°C) compared to rural areas. The spatial trends of the temperature differences can be seen in figure 2. Each dot represents the temperature difference in a specific city. The mean temperature differences for each country are indicated by the stacked bars.

Figure 5: *Photo of the trees through a 720 nm filter*

The reason why the leaves are white at 720 nm lies in the fact that the absorption (a) of the leaves is high in the visible, or photosynthetically active (=PAR) wavelength range between 400 and 700 nm, while the reflectance (r) and transmittance (t) are higher in the near infrared, Figure 6.
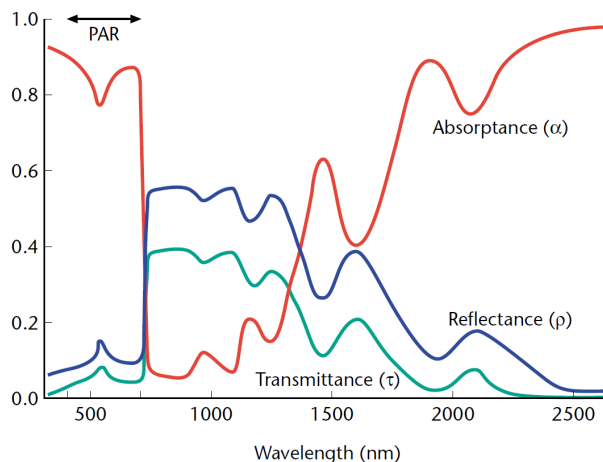
Figure 6: *Absorption, transmission and reflection spectra for 'typical' leaves, source [10]*

The region of spectrum detected by most modern infrared thermal cameras is located from 7 μm to 14 μm, as can be seen in figure 7.
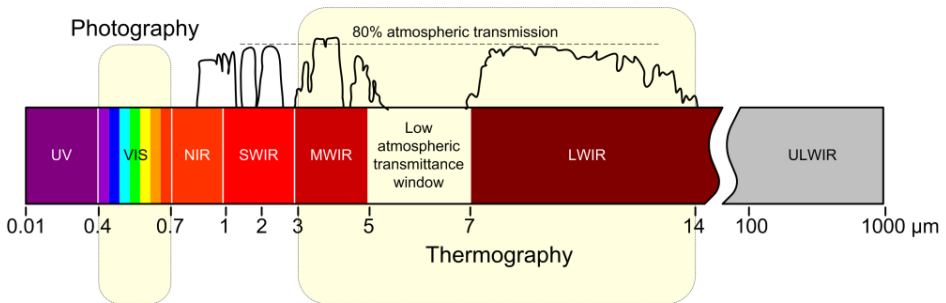
Figure 7: *Classification of thermography in the field of Electromagnetic Radiation.*

The reason why the detectors were developed in the mentioned area is the need to detect the maximum radiation of most objects on earth. In Figure 8. can be see the maximum radiation of the sun, for which our eyes were developed, and the maximum radiation of the earth at approximately 300 °K.
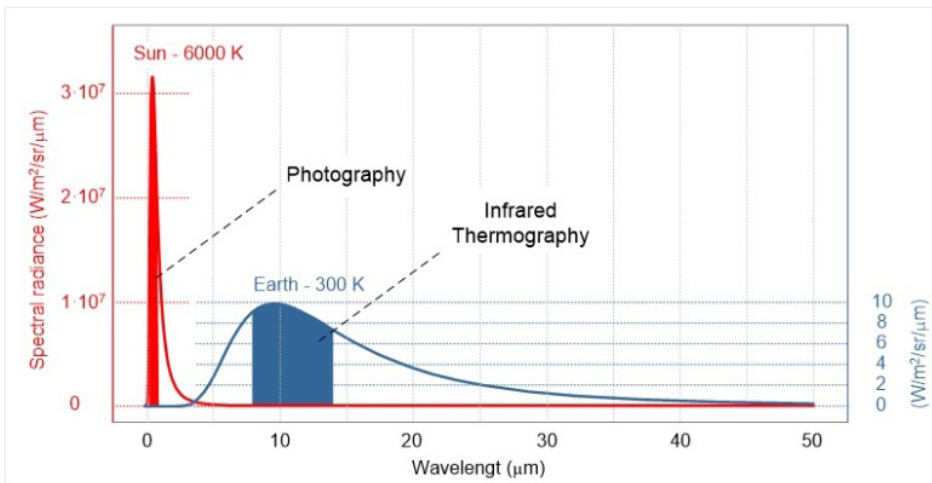
Figure 8: *Comparison of radiation in the visible part of the spectrum and long-wave infrared.*

The summary of everything presented is that, contrary to the general opinion, although it shows the temperature, the infrared thermal camera does not measure the temperature, but the radiation in the infrared part of the spectrum, as can be seen in Figure 9.
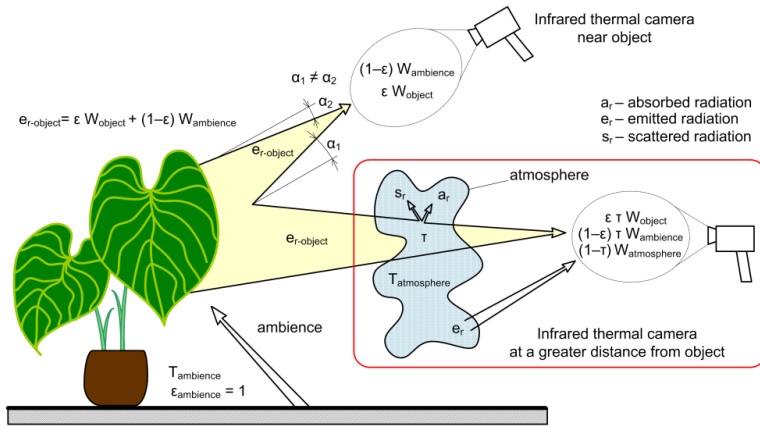
***Figure 9:** Plant radiation that can be detected by the IR camera*

3   WATER STRESS

Water stress in crop growing occurs when the amount of available plant water exceeds or is less than the plant water requirements, i.e., evapotranspiration. Nowadays, in crop production, water stress represents an increasing challenge, because agricultural producers have to compensate for the lack of water in a timely manner through irrigation, or remove excess water from the production area. The problem is increasingly pronounced during the intensification of the negative consequences of climate change, which are manifested in the complex phenomena of periods of intense drought accompanied by extremely high air temperatures and the occurrence of large amounts of precipitation in a very short time, resulting in water scarcity and water-related hazards. As an example, we can highlight the year 2010, when a natural disaster due to flooding and excessive rainfall was declared, resulting in 6.7 million euros of estimated damage. Then two extremely dry years followed, when the 2011 and 2012 drought and heat stresses caused more than 64 and 105 million euros, respectively, in direct losses to agriculture (Marković et al., 2015) [11]. Increasing variations in weather conditions are shown on the example of growing period rainfall and air temperatures deviations from the long-term average (LTA, 1961-1990, Figure 10).
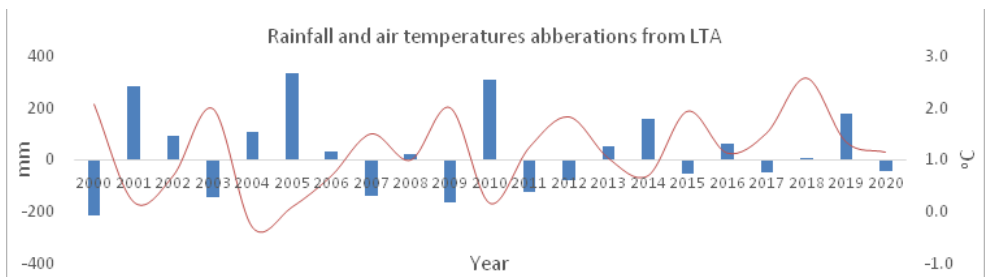
***Figure 10:** Growing season (April-September) rainfall and air temperatures deviations during 2000-2020 period from long-term average (1961-1990)*

From the presented Figure, the aforementioned variations in air temperatures and the irregular rainfall pattern are clearly visible, indicating an increasing need to find solutions to alleviate and to detect water stress in plants. The complex plant growing processes, from germination to the mature stage are affected directly or indirectly by an adequate water supply, whereby different plant species have a certain degree of tolerance to water stress caused by drought or flood (waterlogging) conditions. While the stress caused by drought occurs due to the lack of water easily accessible to the plant and high air temperatures, the stress caused by waterlogging occurs due to intense rainfall, poor drainage systems, soil type and compaction or over-irrigation.

In general, plants respond to water stress with changes to different physiological, morphological and biochemical traits, and it can be studied at a whole plant level as an integrated tissue system, or at the cellular level. Previous study results have shown that drought stress inhibited plant growth significantly, and that the negative physiological response is more pronounced with increasing intensity and duration (Sun et al., 2020, Wu et al., 2022) [12], [13]. As for morphological traits, plants react to drought stress at different growth stages with changes in plant height, fresh weight, dry weight, total biomass as well as yield and yield components. In addition, as a result of the drought, there is a change in the composition of the fruit of the cultivated crop, the content of protein, oil, starch and nutritional elements. The mentioned negative consequences of water stress are important for plant production, growing food and fodder. Furthermore, the negative consequences of water stress are also significant in the cultivation of ornamental plants, where changes in the morphology of flowers, colour and size of flowers and the appearance of the first buds are clearly visible Figure 11, Figure 12.

Figure 11: *Plant height and flower size of Tagetes patula L. in different drought treatments*

Figure 12: *The first bud and flower appearance of a Petunia grown in different drought treatments*

As for water stress caused by flooding, due to the lack of oxygen, there is reduced root growth or complete death, while poor water and nutrient absorption result in lower yield and quality, that is low field production efficiency. As with drought, stress caused by drought results in numerous negative changes in the morphological, biochemical and physiological sense.

Water stress in plant production can be detected and monitored in different ways, i.e., by measuring the water content in the soil with different soil moisture sensors, by estimating stomatal conductivity, leaf turgor, thickness, water content and temperature, cell pressure, etc. Each of the mentioned methods has its advantages and disadvantages. However, the most important thing to point out is that it is important to detect water stress as early as possible, which is a key element of modern plant production, i.e., precision agriculture. In that sense, plant phenotyping, applied to precision agriculture, is a valuable tool for the diagnosis and detection of plant stress, even in the absence of symptoms (Pineda et al., 2021), [14].

4   APPLICATION OF IR THERMOGRAPHY IN THE DETECTION OF WATER STRESS

The accessibility of infrared cameras has led thermography to be a method that can be applied in everyday water stress analysis. The thermal images shown in Figure 13. and Figure 14. were taken on the same date under dryland and irrigated conditions, and represent research from 2015.
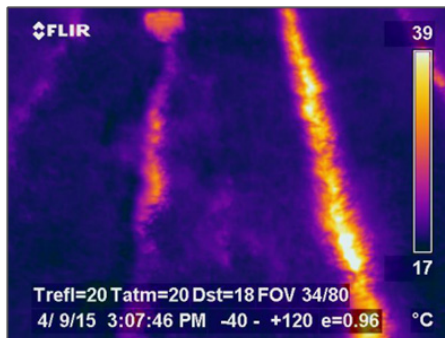
Figure 13: Wheat at dryland, source [15]
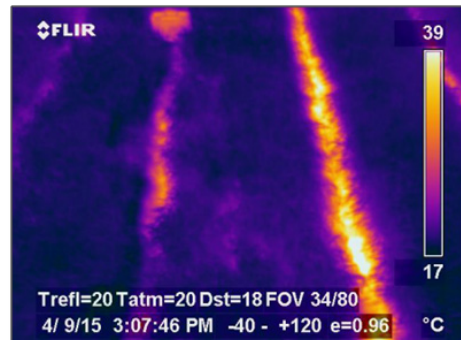
Figure 14: Wheat after irrigation, source [15]

The difference on the thermograms is manifested in the reduction of the temperature of the plants and the soil due to the evaporation of water and the hydration of the plants. Crops which are under water stress tend to have higher temperatures compared to well-hydrated crops, due to transpiration, the process by which plants lose water through their leaves, being reduced under water stress, leading to higher leaf temperatures. Since the time of use of stationary cameras until the realisation of the review presented in the paper, significant changes in interpretation have occurred thanks to the adoption of drones and specialised software support. One of the pioneers in the field of the thermovision detection of water stress is the company Workswell. The WIRIS thermal camera, supported by the DJI S1000 UAV platform and specialised software, can generate temperature maps or thermal indices [16]. These maps can help identify areas of the crop that are experiencing higher temperatures, indicating potential water stress. 5

5   CONCLUSION

The effects of climate change are not only reflected in living conditions, but also in energy requirements, especially in urban areas. The rise in temperature leads to considerable ecological and social consequences. The growing demand for electricity to power air conditioning systems can, and must, be reduced wherever possible. According to the International Energy Agency, air conditioning systems installed after July 1, 2053 must be equipped with a demand response system to manage consumption. South Australia has had such a requirement since 2023. The formation of green islands and the planting of trees and other vegetation have a positive effect on the microclimate and reduce the effects of the urban heat island. Like humans, plants are also sensitive, especially to water stress, which occurs when the amount of available water exceeds or falls short of the plants' water requirements. Infrared thermography is a method of detecting radiation in the long-wave region of the electromagnetic spectrum and is an ideal method for monitoring water stress. Over the last ten years, the prices of the devices have fallen, so that thermography is now used widely, as are thermographic monitoring systems based on drones with special software. The physical background of the detection is based on temperature changes due to water evaporation. Plants under water stress tend to have higher temperatures than well-humidified plants, because transpiration, the process by which plants lose water through their leaves, is reduced under water stress, resulting in higher leaf temperatures. The paper aims to give an overview of the field presented without going into the complexity of control methods to reduce water stress through drainage and irrigation.

References

[1]   **Government of South Australia:** *Department for Energy and Mining, 'Demand response capability requirements for installation of all air conditioning types',* Technical Regulator Guideline, Energy and Technical Regulation, 2023

[2]   **C. Camarasa**, Public webinar - IEA's Energy Efficiency 2023 Report: Key findings and a chance to discuss with Lead Authors, Odyssee-Mure, 7 December 2023

[3]   **International Energy Agency – IEA**, Available: https://www.iea.org/data-and-statistics/data-tools/energy-statistics-data-browser?country=CROATIA&fuel=Energy consumption&indicator=TotElecCons (April 30, 2023)

[4]   **V. Monteiro, M. & H., Phillip & Morison, J. & D., Kieron,** *The role of urban trees and greenspaces in reducing urban air temperatures*, 2019

[5]   **S. Önder, A. Akay**, *The Roles of Plants on Mitigating the Urban Heat Islands' Negative Effects*, International Journal of Agriculture and Economic Development, ISSN : 2331-0200

[6]   **J. Schwaab, R. Meier, G. Mussetti, et al.** *The role of urban trees in reducing land surface temperatures in European cities*. Nat Commun 12, 6763 https://doi.org/10.1038/s41467-021-26768-w, 2021

[7]   **E. Massaro, R. Schifanella, M. Piccardo, et al.** *Spatially-optimized urban greening for reduction of population exposure to land surface temperature extremes,* Nat Commun 14, 2903, https://doi.org/10.1038/s41467-023-38596-1, 2023

[8]   **H. Glavaš, M. Hadzima-Nyarko, I. Haničar Buljan, T. Barić**, *Locating Hidden Elements in Walls of Cultural Heritage Buildings by Using Infrared Thermography*. Buildings 2019, 9, 32. https://doi.org/10.3390/buildings9020032

[9]   **Č. Livada, H. Glavaš, A. Baumgartner, D. Jukić**, *The Dangers of Analyzing Thermographic Radiometric Data as Images*, Journal of Imaging 9, no. 7: 143. https://doi.org/10.3390/jimaging9070143 2023

[10]   **H. G. Jones, Hamlyn, E. Rotenberg**, *Energy, Radiation and Temperature Regulation in Plants*, In eLS, John Wiley & Sons, Ltd (Ed.). https://doi.org/10.1038/npg.els.0003199, 2001

[11]   **M. Marković, M. Josipović, V. Tadić, V. Zebec, M. Josipović, V. Filipović,** *Efficiency of maize irrigation scheduling in climate variability and extreme weather events in eastern Croatia*. Journal of water and climate change, 6(3): 586-595, 2015

[12]   **Y. Sun, C. Wang, H.Y.H. Chen, R. Honghua**, *Response of Plants to Water Stress: A Meta-Analysis*. Front. Plant Sci., 11: 978, 2020

[13]   **J. Wu, j. Wang, W. Hui, F. Zhao, P. Wang, C. Su, W. Gong,** *Physiology of Plant Responses to Water Stress and Related Genes*: A Review. Forests, 13, 324, 2022

[14]   **M. Pineda, M. Barón, M.-L. Pérez-Bueno,** *Thermal Imaging for Plant Stress Detection and Phenotyping*. Remote Sens., 13, 68, 2021

[15]   **M. Bhandari**, *Use of infrared thermal imaging for estimating canopy temperature in wheat and maize*, Ms Thesis, West Texas A&M University, Canyon, Texas, August, 2016

[16]   **Workswell**, *WIRIS Agro*, Available: https://www.drone-thermal-camera.com/detection-of-water-stress-cereals-crops-with-thermal-camera/#, (April 30, 2023)

Journal of Energy Technology

CONSERVATION OF FISH MIGRATIONS AT HYDROELECTRIC POWER PLANTS: FISH PASSAGE SYSTEMS AS AN ENVIRONMENTALLY RESPONSIBLE MEASURE

OHRANJANJE RIBJIH MIGRACIJ OB HIDROELEKTRARNAH: PZVO KOT OKOLJSKO ODGOVOREN UKREP

Boštjan Pišotek[1], Sandra Velkovski [2]

Abstract

The geostrategic situation in the world is a stark reminder that, for any country seeking to be sovereign, it is essential to strengthen the degree of energy and food self-sufficiency as soon as possible, all the while also ensuring sustainable environmental and social development. In terms of renewable energy sources, Slovenia has the greatest privilege in being able to utilise hydropower and wood biomass for energy uses. The paper discusses the importance of implementing multipurpose and goal-oriented projects such as hydropower plants (HPPs), which fulfil a number of strategies set by the state and local communities. Since every human intervention in the environment has certain impacts, the paper shows how synergistic effects can be created between environmental protection and energy sector development through responsible environmental planning and implementation of the best possible measures, drawing from a practical example of the multipurpose construction project of HPPs on the lower course of the river Sava. The paper addresses the issue of fish migration and barriers in watercourses, presenting the current situation in Slovenia and worldwide. It also examines the success of fish passes at HPP Arto-Blanca, based on several years of monitoring. Such passes enable fish to

---

[1] HESS, d.o.o., Investment Department, Cesta bratov Cerjakov 33a

[2] HESS, d.o.o., Environmental Department, Cesta bratov Cerjakov 33a

migrate past hydropower plants, maintain healthy fish populations, preserve genetic diversity, and ensure the connectivity and preservation of the entire aquatic ecosystem. The example of the future Mokrice hydropower plant illustrates the trend and commitments in the planning of such passes in the future.

Povzetek

Geostrateška situacija v svetu opozarja, da je za državo, ki želi biti suverena, nujno, da čim prej okrepi stopnjo samooskrbnosti z energijo in hrano ob sočasni skrbi za vzdržni okoljsko-družbeni razvoj. Slovenija ima na področju obnovljivih virov energije največji privilegij v koriščenju hidroenergije in lesne biomase. V prispevku je obravnavan pomen izvajanja večnamenskih in ciljno usmerjenih projektov, kot so hidroelektrarne, ki izpolnjujejo več zadanih strategij države in lokalnih skupnosti. Upoštevajoč dejstvo, da ima vsak človekov poseg v prostor določene vplive, je na praktičnem primeru večnamenskega projekta izgradnje HE na spodnji Savi prikazano, kako se lahko z odgovornim okoljskim načrtovanjem in izvedbo najboljših možnih ukrepov ustvarijo sinergijski učinki med varovanjem okolja in razvojem energetike. Predstavljena je tematika ribjih migracij in pregrad na vodotokih, prikazano aktualno stanje v Sloveniji ter po svetu in na podlagi večletnih monitoringov obravnavan primer uspešnosti ribjega prehoda pri HE Arto-Blanca. Tovrstni prehodi omogočajo ribam: migracijo mimo hidroelektrarn in ohranjajo zdrave populacije rib; vzdrževanje genetske raznolikosti; povezanost in ohranitev celotnega vodnega ekosistema. Na primeru bodoče HE Mokrice so predstavljeni trend in obveze pri načrtovanju tovrstnih prehodov v prihodnje.

1   INTRODUCTION

The geostrategic situation in the world is a stark reminder that, for any country seeking to be sovereign, it is essential to strengthen the degree of energy and food self-sufficiency as soon as possible, all the while also ensuring sustainable environmental and social development. In terms of renewable energy sources, Slovenia has the greatest privilege in being able to utilise hydropower and wood biomass. At the turn of the millennium, Slovenia's political strategy in the context of energy and climate change made bold strides towards increasing the share of electricity generated from renewable energy sources (RES). The actual effects of the special Act adopted in 2000 – "Conditions of the Concession for Exploitation of the Energy Potential of the Lower Sava River Act" (abbr. ZPKEPS) – are today reflected in the fact that Slovenia produces as much as 37% of electricity from RES. Hydropower plants (HPPs) account for the largest share, specifically 92%. The 4,880 GWh of net electricity production from HPPs in 2021 represents a 60% increase compared to the period 25 years ago *[1]*.

The HPP construction project in the lower course of the Sava is designed as a multipurpose project, the positive effects of which are manifested mainly in improved flood safety, development of the environment and biodiversity, agriculture, tourism, sports and recreational activities, and local and national infrastructure. It is also necessary to highlight the project's important contribution to the implementation of sustainable development, increasing the share of renewable energy sources and fulfilling Slovenia's commitments to the European Union (EU), maintaining competitiveness and strengthening Slovenia's industry, ensuring higher employment levels, and contributing to revenues for the national budget and the budgets of local communities *[2]*.

For centuries, man has reconfigured and blocked watercourses continually, with the aim of

facilitating work, improving the quality of life, and making the energy of water do the physical work for him. In the area of present-day Slovenia, the energy of water was used predominantly to drive sawmills, pumps and grain mills. The latter began to appear there in the 9th century (Kos, 1906), and became widespread in the 12th and 13th centuries (Bogataj, 1982), with around 1,700 of them in operation by the end of the 19th century. The first hydroelectric power plants (HPPs) began to be built on the river Drava more than 100 years ago.

The construction of barriers on rivers therefore affected the migration routes of aquatic organisms and ecosystems. The problem of barriers and fish migration is much more widespread globally than it is in Slovenia. In the past, rivers in the European countries Spain (Cortes-La Muela Dam), Germany (Rappbode Dam, Bleiloch Dam, Eder Dam), France (Grand'Maison Dam), Portugal (Tamega Giga Battery Dam) and Switzerland (Grande Dixence Dam, Luzzone Dam) were outfitted with large barriers or HPP reservoir dams with depths exceeding 100 m and storing some 100 million cubic metres of water. Such impoundments can cause extensive changes in aquatic ecosystems, leading to declines in fish populations and loss of biodiversity.

Compared to abroad Slovenia practically does not have such barriers, as we have developed run-of-the-river reservoir HPPs with depths varying up to around 20 m and only storing some 10 million cubic metres of water. During the construction of the HPPs on the lower course of the Sava a number of nature conservation measures were taken into account, in order to reduce the impact of barriers on fish migrations and ecosystems. One of the key approaches was the development of run-of-the-river HPPs, which, with flow rates above 1,000 m³/s, allow a river to flow freely over the HPP and enable the downstream migration of fish. In addition, other important solutions were also implemented at the HPPs Arto-Blanca, Krško and Brežice, such as fish passes (fishways) and other structures (spawning grounds, inlets, resting pools, quiet areas, replacement habitats) that help aquatic organisms and other animal species to overcome obstacles caused by barriers in the river. As part of the HPP chain on the lower course of the Sava, special attention was also placed on the planning of nature conservation measures, which allow the intervention in the environment to have the smallest possible impact [3][4], and which were approved by nature conservation, biology, ichthyology, water science, and technical specialists.

2 EXAMPLE OF GOOD PRACTICE – FISH PASS AT HPP ARTO-BLANCA

The Arto-Blanca hydropower plant was built in 2008 and went into operation in 2009. Next to the hydropower plant, a fish pass was built, the first of its kind to be situated next to an HPP on the Sava. The fish pass was designed with the aim of allowing the passage for all species of fish found in the lower course of the Sava. Ichthyology specialists and the Fisheries Research Institute of the Republic of Slovenia (ZzRS) were involved in the project from the outset.

The fish pass at HPP Arto-Blanca consists of a close-to-nature section imitating natural watercourses, and a technical inflow section made up of two branches and designed to regulate the flow with a double-gate system. The fish pass is of vital importance, particularly for the fish species that migrate over long distances in search of food and spawning grounds within the watercourse. These species include the common nase, common barbel, cactus roach, chub, ide, asp, vimba bream, carp bream, pike, huchen, brown trout and ruffe.

Figure 1: *Fish pass next to HPP Arto-Blanca, allowing the migration of aquatic organisms.*

By building fish passes or fishways, we allow the fish to pass smoothly past the dams over the long term, which prevents the fragmentation of populations, enables gene flow between populations, and, therefore, preserves the species` diversity in inland waters, while also allowing us to follow and meet the requirements of European and Slovenian legislation.

Standardised evaluations of the efficiency of the fish pass at HPP Arto-Blanca were carried out in 2009 *[5]*, 2010 *[6]*, 2012 *[8]*, 2015 *[9]* and 2022 *[11]*. In the close-to-nature section, the fish sampling was carried out using electricity or electrofishing, and in the technical part, in addition to the above method, sampling was also performed using creels (Figure 2, Figure 3). Already after the first two years of operation, it has become clear that the fish pass operated well and fulfilled its function fully *[6]*. The fish pass was recognised as an example of good practice in 2013, and was also cited in the report of the International Commission dealing with the Danube basin – the International Commission for the Protection of the Danube River (ICPDR) *[10]*.

The fish pass was negotiated demonstrably along its entire length by the common nase, chub, brown trout, vimba bream, cactus roach, common barbel, carp bream and five species from Appendix II of the Habitats Directive: the Danube gudgeon, white-finned gudgeon, Danube streber, spined and Balkan loach *[6], [7]*. In all the monitoring activities to date, a total of 35 species of fish and one species of lamprey have been recorded in the pass, and the functionality of the spawning grounds has also been confirmed. Eggs of the common nase were also observed attached to the stones in the fishway, which goes to show that the common nase spawned inside the very fishway *[6]*.

Figure 2: *Electrofishing in the fishway – close-to-nature section [8].*

Figure 3: *Deployment of a creel in the technical section of the fish pass [8].*

Species such as the common rudd, tench, Kessler's gudgeon, zander, burbot, white bream, Danube gudgeon and Danube streber were rare in this part of the Sava even before the construction of the HPP *[6], [8], [15]*. The fact that the above fish species were observed during previous run-of-the-river reservoir monitoring activities upstream and downstream of the HPP Arto-Blanca fish pass suggests that they were able to pass upstream past the dam structure, but, due to their rarity, they were not recorded during the fish pass samplings, or were only recorded during some samplings. Here, it needs to be pointed out that the incidence or observation of some species may also have been affected by the time of the year in which the sampling was carried out *[15]*.

The sampling with electrofishing in 2009, for example, was carried out over a period of 3 fieldwork days in the autumn, for the first time in September, when the fishway was still in trial operation, followed by the second and third times in November and December. In 2010, electric sampling was carried out over a period of 3 fieldwork days in March, June and October *[6]*, in 2012 over a period of 3 fieldwork days in May and September *[8]*, and, in 2022, over a period of 2 fieldwork days in May and September *[11]*. Creel sampling was carried out over a period of 8 days in July, September and October 2010 *[6]*, 10 days in April, June, July, August, September and November 2012 *[8]*, 5 days in March, May, June, September and November 2015 *[9]*, and 6 fieldwork days

in April, May, June, July, September and October 2022 *[11]*.

In 2022, during the upstream passage along the fish pass, the highest number of species were recorded in the spring during spawning, and the lowest in the autumn. The passage along the fish pass is, therefore, connected most closely to the spawning migration, where sexually mature specimens move upstream between individual run-of-the-river reservoirs to spawning grounds, where the conditions for spawning in the fish pass are favourable for all the present species, allowing them to spawn inside the pass as well. The results of the monitoring activities confirmed that all the potamodromous fish species present in this stretch of the Sava can travel along the entire length of the fish pass, and that they also use the pass outside the spawning season. Based on several years of monitoring, it has been confirmed that the fish pass fulfils its function effectively, and is a key measure that allows the settlement and long-term survival of fish populations in the run-of-the-river reservoirs of hydropower plants.

3   PLANNED MEASURES TO PRESERVE FISH MIGRATIONS AT HPP MOKRICE

In order to ensure connectivity, a fish pass was already included in the project solutions during the Strategic Environmental Assessment (SEA) process, and followed the designs of the already operational fish pass next to HPP Arto-Blanca, which has been confirmed to be effective in practice *[7], [10]*. During the Environmental Impact Assessment (EIA) process, based on the guidelines for introducing measures to ensure fish migration *[12]*, significant progress has been made towards improving connectivity solutions. Based on the recommendations from the guidelines, it makes sense to build 2 fish passes on larger rivers (wider than 100 m) during the construction of HPPs, specifically one fish pass on either side of the river. In accordance with this requirement, an additional fish pass or diversion channel on the left bank of the Sava was added as part of the modification of Quiet Area 4 (MO4). Both fish passes are designed so as to achieve two essential objectives, i.e., passage for all fish species past the dam structure and establishment of conditions for their spawning. An essential element of the fish pass is a close-to-nature section ,designed in the form of a close-to-nature river channel.

Fish Pass 1, on the right bank, is 655 m long, and has an average longitudinal gradient of 1.3%, the total length of 6 spawning grounds in the close-to-nature section is 180 m, and all spawning grounds are the same length and more than 9 m wide. The spawning grounds are designed in the form of two parallel corridors, so that the spawning of lithophilic spawners is enabled along one bank, while along the other bank fish can pass upstream in all sections.

Figure 4: *Fish Pass 1 on the right bank next to HPP Mokrice.*

Fish Pass 2, on the left bank, or the diversion channel, has a close-to-nature section 1,260 m long with an average longitudinal gradient of 0.65%, with 4 spawning grounds with a combined length of 240 m, 3 resting pools with a combined length of 115 m, hiding spots, pools, and habitat structures. Adequate flow rates will be provided in both fish passes, enabling water flow velocities suitable for the migration of all species of fish in the area.

The spawning grounds will, thus, be located close to where the fish enter the pass, which is essential for the spawners during the spawning season. Stone-lined spawning grounds are provided, with conditions suitable for lithophilic spawners. Four types of structures are defined that represent different habitats: inlet chutes, spawning grounds, passages and pools. Fish travelling through the pass will be able to continue their journey up the run-of-the-river reservoir, and will also be able to access the Krka. It should be noted here that the Mokrice HPP is designed as a run-of-the-river HPP, where the water in the run-of-the-river reservoir can be exchanged up to 6 times a day. When constructed, HPP Mokrice will take over the function of ensuring the daily natural flow rate on the border profile within the HPP chain on the Sava. Therefore, there is no defined ecologically acceptable flow rate for HPPs on the lower course of the Sava, as is typically determined for derivative power plants. The following section provides an explanation behind the determination of the flow rates in the fish passes.

Figure 5: Fish pass on the left bank, developed during the Environmental Impact Assessment (EIA) phase.

The basic flow in the fish pass was determined according to the biological needs of migratory fish species that are located in, or that migrate in the river Sava in the area of the barrier inhabited by the fish of the barbel zone. The determination of the geometric and hydraulic variables in the fish pass, including the flow rate, is based on taking into account the following conditions, as provided in various authoritative manuals and Standards for the Danube region; ICPDR *[10]*, DWA-M-509 , BAW BfG Guideline, and others *[13], [14]*:

- the weakest swimmers of all age groups above 1+ are taken into account by determining the maximum permissible velocity of the water flow occurring in the narrowed sections, in the vertical slots of the compartmented section, and in the openings between the rocks of the close-to-nature ramps;

- in the vertical slots of the technical part of the inflow facility, the maximum permissible velocity is Vmax = 1.1 m/s. The velocity was determined through hydraulic model research at the Institute for Hydraulic Research;

- in the openings/gaps between the rocks on the ramps in the close-to-nature channel, the maximum permissible velocity of the water flow is Vmax = 0.6 m/s;

- the largest fish from the set of relevant fish species are taken into account, by considering the recommended minimum widths of narrowed sections and the minimum water depth

for them, taking into account the permissible maximum water velocity in the narrowed sections;

• the level of the upper and lower water at the barrier and the fluctuation of levels for a period of 300 days per year are taken into account, i.e., according to the recommendations of the ICPDR for the Q flows of the Sava between Q30 and Q330, i.e., for the period for which the passability, functionality and efficiency of the fish pass is ensured. This defines the height difference in the gaps between the chambers in the inflow technical facility, and on the ramps between the pools in the close-to-nature section.

Flow rate in Fish Pass 1: The basic flow rate in Fish Pass 1 is 800 l/s. Three operating flow modes with different flow rates are envisaged for different cases of ecological needs in the close-to-nature section of the fish pass in different seasons. At different flow rates, different water depths are established in the fish pass, while the water flow velocities are maintained.

Flow rate in Fish Pass 2: In the Technical Guidelines of the Fisheries Research Institute of Slovenia, a range of acceptable or optimal flow rates were determined, to ensure the functionality of all structures in this fish pass. The range of flow rates was determined between 2 m³/s and 3 m³/s, with the fact that Fish Pass 2 is already fully functional at a flow rate of 2 m³/s, which means that, in this case, both objectives have been achieved: passability and spawning for lithophilic spawners. The central technical part of the inflow facility is dimensioned to support a flow rate of 800 l/s. The difference to the full flow rate of 2 m³/s will be provided by a parallel channel next to the central part of the inflow facility, which will ensure the supply of additional water flow directly to the close-to-nature section of Fish Pass 2.

4   CONCLUSION

The energy sector and environmental protection have undergone significant changes over time, reflecting advances in technology and a growing concern for sustainable development. A historical review of the development of hydropower projects reveals changes in the approach to HPP construction, particularly regarding the inclusion of environmental measures such as fish passes. Until the end of the 1990s, HPPs and other dams were built without fish passes, which resulted in the fragmentation of fish populations and had a negative impact on the biodiversity of aquatic ecosystems. With advances in the knowledge of ecosystems, projects began to appear that already included environmental aspects at the planning stage. HPP Arto-Blanca, built in 2008, represents an important turning point in this regard, as it includes the very first fish pass on the Sava.

Evaluations of the efficiency of the fish pass at HPP Arto-Blanca yielded positive results. Monitoring has confirmed that all the fish species present in the area have negotiated the fish pass successfully, affirming the efficiency of the fish passes and their importance for the preservation of fish populations. A total of 35 species of fish and one species of lamprey were recorded in the fish pass, which confirms its functionality and allows fish species to pass between individual run-of-the-river reservoirs.

In the designing of the latest hydropower plant, HPP Mokrice, experience from past projects was taken into account, leading to the inclusion of two fish passes in the project. The basic flow

rate in the fish pass was determined according to the biological needs of migratory fish species, ensuring that the efficiency and functionality of these passes are in accordance with European and Slovenian legislative requirements.

The shift from the construction of HPPs without fish passes to the inclusion of advanced fish passes in modern projects such as HPP Arto-Blanca, HPP Brežice and HPP Mokrice, reflects significant progress in terms of the integration and synergy of the energy sector and environmental protection. These projects not only contribute to the production of clean energy, but also support the preservation of natural habitats and biodiversity, which is crucial for sustainable development, the future of our ecosystems and the mitigation of climate change.

References

[*1*]   **Energy Agency:** Report on the Energy situation in Slovenia 2021. Available: https://www. energetika-portal.si/fileadmin/dokumenti/publikacije/agen_e/porae_2021.pdf (28. 8. 2023)

[*2*]   **B. Pišotek, A. Rajh:** Hydropower Plants as a Significant Water Management Project - Multiplier Effects of Construction", Conference 26th MVD, 2015

[*3*]   **B. Pišotek:** *Socially responsible way of water management, Slovenian Fishing Newsletter* Ribič, 1–2/2020, 11–12. Volume LXXIX. ISSN 0350-4573, 2020. Available: https://ribiska-zveza.si/downloads/ribic_1_2_2020_3eJoO.pdf (18. 8. 2023)

[*4*]   **B. Pišotek, S. Jeršič:** *The strategic importance of water for the development of Slovenia – What is the contribution of hydropower plants in mitigating the effects of climate change and their importance for the society of the future?*, 3rd Slovenian Water Conference, Ptuj, 2023

[*5*]   **D. Zabric:** *Ichthyological survey at HPP Boštanj and HPP Blanca*, Fisheries Research Institute of Slovenia, 2009

[*6*]   **D. Zabric:** *Ichthyological survey at HPP Boštanj and HPP Blanca: Monitoring of the HPP Blanca fishway*, Fisheries Research Institute of Slovenia, 2010

[*7*]   **D. Zabric:** *Fish pass at HPP Blanca – an example of good practice*, Life to Water, a compendium of papers, National Council, 2011

[*8*]   **D. Zabric:** *Ichthyological survey at HPP Boštanj and HPP Blanca in 2012*, Fisheries Research Institute of Slovenia, 2012

[*9*]   **D. Zabric:** *Ichthyological survey at HPP Arto-Blanca in 2015: Fish pass monitoring*, Fisheries Research Institute of Slovenia, 2015

[*10*]   **ICPDR**: *Hydropower Case Studies and Good Practice Examples: ANNEX to Guiding Principles on Sustainable Hydropower Development in the Danube Basin*, ICPDR – International Commission for the Protection of the Danube River, 2013

[*11*]   **S. Podgornik:** *Ichthyological monitoring at HPP Arto-Blanca in 2022*, NEPO, 2022

[*12*]   **S. Schmutz, C. Mielach:** *Measures for ensuring fish migration at transversal structures*, ICPDR, 2013

[*13*]   **EC:** *Guidance on The requirements for hydropower in relation to Natura 2000,* 2018

[*14*]   **M. Bombač, G. Novak, P. Rodič, M. Četina:** *Numerical and physical model study of a vertical slot fishway*, J. Hydrol. Hydromech., 62, 2014, 2, 150–159, DOI: 10.2478/johh-2014-0013, 2014

[*15*]   **S. Podgornik, A. Jenič, K. Pliberšek, M. Govedič, M. Bertok:** *Ichthyological research of the Sava and its tributaries from Krško to the border*, Fisheries Research Institute of Slovenia, 2009

Nomenclature

EIA	environmental impact assessment
HPP	hydropower plant
SEA	strategic environmental assessment
MO	quiet area
RES	renewable energy sources

Journal of Energy Technology

CONFIGURATION OF A FLAT ROOF SOLAR POWER PLANT FOR MAXIMUM ELECTRICITY PRODUCTION

KONFIGURACIJA SONČNE ELEKTRARNE NA RAVNI STREHI ZA MAKSIMALNO PROIZVODNJO ELEKTRIČNE ENERGIJE

Neja Hadžiselimović[R]

Abstract

Commercial solar power plants are often installed on larger industrial, warehouse and commercial buildings. Modern prefabricated constructions of such buildings dictate architectural solutions involving flat roofs, which are particularly suitable for the installation of larger solar power plants. This research investigates which configuration of solar module installation and which inclinations are suitable for implementation on a flat roof to achieve maximum annual electricity production. It aims to determine the maximum annual production per unit area and per installed power of the solar modules. The simulation results are conducted for all months of the year, and for the geographic latitude and longitude of the town of Lenart in Slovenia.[1]

Povzetek

Komercialne sončne elektrarne se velikokrat postavljajo na večje industrijske, skladiščne in trgovske objekte. Moderne montažne konstrukcije tovrstnih objektov narekujejo arhitekturne

---

[R] 1 Corresponding author: Neja Hadžiselimović, II. gimnazija Maribor, Trg Miloša Zidanška 1, 2000 Maribor, Slovenia, Tel.: +386 40 349 536, E-mail address: neja.hadziselimovic@druga.si

rešitve v izvedbi ravnih streh, ki so posebej primerne za postavitev večjih sončnih elektrarn. Tako je cilj članka raziskati optimalno konfiguracijo sončnih modulov na ravni strehi z namenom doseganja maksimalne proizvodnje električne energije. V tem delu je izvedena raziskava glede tega, katera orientacija sončnih modulov in kateri nakloni so primerni za izvedbo na ravni strehi s ciljem, da bo dosežena maksimalna letna proizvodnja električne energije. Gre za določitev maksimalne letne proizvodnje na površino in na inštalirano moč modulov. Simulacijski rezultati so izvedeni za vse mesece leta ter za geografsko širino in dolžino mesta Lenart v Sloveniji.

1   INTRODUCTION

As indicated by the study "The Limits to Growth" from 1972 *[1]*, modern society faces global problems that lead increasingly to an imbalance between the ecosphere and the socio-technosphere, essentially leading to an ecological crisis. Consequently, within the framework of sustainable development, the central focus of modern society has become the green transition *[2,3]*, which does not rely on excessive consumption of natural resources and overburdening the environment. The goal is sustainable development, which aims to meet the needs of the present without compromising the environment and ability of future generations to meet their own needs.

In this millennium, green technologies that utilise renewable energy sources are becoming increasingly popular in practice. These sources include sea energy, bioenergy, hydro-, wind, geothermal-, and, notably, solar energy. Due to the development of society, the increased standard of living and because of facts regarding global warming *[4,5]*, the need for electrical energy is increasing, especially for cooling and heating buildings as well as the introduction of electric mobility. Thus, society also harnesses solar energy through solar power plants, which represents one of the possible green solutions, provided the power grid infrastructure is upgraded appropriately with smart solutions and adequate storage systems. However, it is a fact that such power plants cannot be installed just anywhere, as this would lead to harmful environmental consequences, including habitat loss, threats to biodiversity, and loss of agricultural land intended primarily for food production *[6]*. Agrovoltaics, which combines food and electricity production while adding value to agriculture, is emerging as one of the solutions *[7,8]*. In agrovoltaics, solar modules are installed above crops, providing favourable conditions for the growth of certain plants compared to full sunlight, which will be extremely important in the future, because of the increase in temperatures due to global warming, especially for rational use of water in agriculture. In the desire to reduce pressure on the environment, it will, therefore, be very important to use areas already designated for the purpose of the additional production of electricity. In this context, the best possible placement of solar power plants with minimal environmental impact is on the roofs of existing buildings, which can be categorised as residential and industrial. In the case of single-family and multi-family buildings in Slovenia, roofs are most commonly gabled, or, more recently, mono-pitched, which is often used in modern construction. For industrial buildings, particularly large warehouses and production halls, flat roofs are used predominantly. Since there are many such large buildings, they present an excellent opportunity for installing solar power plants. The question that arises and the primary issue addressed in this paper is how best to utilise large flat roofs to electricity production. Proper placement of solar modules on flat roofs can maximise electricity production. In studying the problem of maximising solar power production on a flat roof, it is necessary to consider that flat roofs are not entirely flat, but have a minimal slope for proper drainage of meteorological water. The minimum recommended slope

of a flat roof is at least 1.19° *[9]*. In seeking the ideal placement of solar modules, it is essential to consider their tilt relative to the flat roof, their orientation, and the spacing required to avoid shading between rows of solar modules. All these factors depend on the basic principles of solar radiation and the microclimatic conditions at a specific latitude, as presented in the following sections.

To discuss radiation, we must first mention the sun. It is a star that enables our existence and is the source of almost all the energy received by the Earth. The reason for such a large amount of solar radiation is the nuclear fusion reaction, which converts hydrogen into helium, releasing an enormous amount of energy. Of this, only 49% of the radiation is absorbed by the ground, while the rest is reflected by clouds, back into space, or from the surface *[10]*.

All the radiation received by the Earth from the sun is called global radiation, which consists of two components - direct and diffuse radiation. The first comes directly from the sun, while the latter comes from all parts of the sky. The amount of radiation on the earth's surface depends on the angle of incidence of the sun's rays. This is the angle between the sun's rays and the normal to the inclined surface. It depends on the time of year and the geographic latitude of the observed location. It is a factor that influences the amount of electricity produced by a solar power plant directly. The angle of incidence of the sun's rays α depends directly on the hour angle h, declination δ and longitude L. All these angles are marked in Fig. 1 *[11]*.
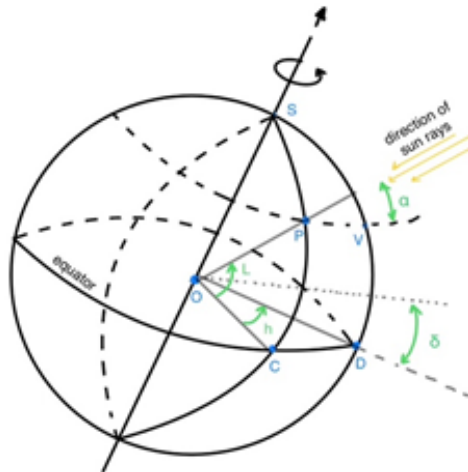
Figure 1: *Definition of hour angle, latitude and declination [12]*

If those angles are known, it is possible to calculate the incident angle of the sun's rays using the cosine theorem (triangle SPV Fig. 1) according to the following equation *[12]*:

$$\cos(90° - \alpha) = \cos(90° - L)\cos(90° - \delta) + \sin(90° - L)\sin(90° - \delta)\cos(h) \qquad (1.1)$$

The equation can be simplified further:

$$\sin(\alpha) = \sin(L)\sin(\delta) + \cos(L)\cos(\delta)\cos(h) \qquad (1.2)$$

All other correlations between the laws of solar radiation and the production of electricity from a solar power plant, such as daily declination, longitudinal correction, hour angle, local zenith, sun altitude, sun azimuth, etc., are already generally known from different literature *[11]*. The essence of the above is that the angle of incidence of the sun's rays changes over the months, which means that the amount of electricity produced by the solar power plant also changes. However, the focus of this paper is to maximise the total annual electricity production, and to determine the optimal placement for achieving this goal.

Nonetheless, the first step in finding the configuration of the solar power plant is determining the orientation of the solar modules, with three main options: horizontal placement, orientation towards the south (in the northern hemisphere), and east-west orientation. If the solar modules are placed on the roof and oriented south, the maximum electricity production occurs in the middle of the day when the sun's rays are perpendicular to the solar modules, with reduced electricity production in the morning and evening. An East-West orientation enhances energy production during the morning and evening hours, while also allowing for the installation of additional solar modules on the roof, thereby maximising the use of available space. Solar modules placed horizontally on a large flat roof are not used commonly in practice, because snow, pollen, dust and other particles accumulate on them, reducing the amount of produced electricity significantly. To avoid this issue solar modules are tilted at an angle, to maximise annual electricity production. The optimal tilt angle varies between winter and summer, due to the changing angle of the sun's rays throughout the year. In fixed solar power plants the tilt angle cannot be adjusted, so the optimal orientation is generally achieved by choosing an angle close to the geographic latitude and azimuth angle, facing north in the southern hemisphere and south in the northern hemisphere. Therefore, the tilt angle must be determined according to the location where the solar power plant will be installed. In this paper, all simulations are related to the location of Lenart, Slovenia, with the coordinates 46.5834° N and 15.8262° E. Due to the angle of incidence of the sun's rays, the distance from the equator, i.e., geographic latitude, is a significant factor. For the location of Lenart, a tilt angle of 38,5° is optimal for south-orientated solar modules to achieve maximum annual electricity production in a fixed solar power plant *[13]*.

The main issue with tilting solar modules on a flat roof is shading, which results in only the first row producing the maximum possible electricity. If the distance between the rows is too small, each preceding row will shade the subsequent ones at certain times. Although the tilt angle can increase electricity production, it simultaneously causes shading, making it essential to find an optimal balance between the tilt angle and spacing. Increasing the distance between the solar modules reduces shading, but also reduces the number of solar modules on the roof, which, again, decreases electricity production.

2   METHODOLOGY

2.1   The main components of the solar power plant and used software package

As emphasised repeatedly, the primary goal of this research is to determine the optimal placement of solar modules on a large flat roof, to ensure that the solar power plant produces the maximum amount of electricity annually. To explore the optimal spacing, orientation and tilt

of the solar modules, it was necessary to create a simulation model. There are many different solar plant design software tools available, such as Aurora Solar, OpenSolar, Helioscope, Solo and SolarEdge, the latter of which was chosen for the research in this paper. SolarEdge is a global company which provides smart energy technology, especially in seeking opportunities to harness renewable energy sources. Since its inception, SolarEdge has been at the forefront of developing new solar technologies that enhance the efficiency and reliability of photovoltaic systems *[14]*. With its comprehensive services, it offers support to both planners and users, with their free solar design tools being particularly useful for this research. Among these tools is SolarEdge Designer, which provides users with satellite HD images, AI-assisted 3D modelling, irradiance mapping, shading analysis, automated electrical calculations to enhance electricity production, and energy simulations and forecasts *[15]*.

The above reasons explain the choice of SolarEdge Designer, in which the simulation model was created. Subsequently, it was necessary to select the main components of the solar power plant within the program, which were used consistently across all configurations of the solar power plant, and are presented below.

A solar module type Himalaya G10 Series from Huasun Manufacturer with 108-cell bifacial with hetero junction technology *[16]* was used for all the simulations. The modules are 1722 mm long, 1134 mm wide and 30 mm high. The nominal data of the solar module used in this paper are presented in Table 1, where P_{max} represents the maximum power of the solar module, *EFF* is the efficiency, U_{mp} is the optimum operating voltage, I_{mp} is the optimum operating current, V_{oc} is the open circuit voltage, I_{sc} is the short circuit current, *m* is the solar module mass and IP is the ingress protection.

Table 1: *Nominal data of solar module HS-182-B108 D430*

P_{max} (W)	EFF (%)	U_{mp} (V)	I_{mp} (A)	V_{oc} (V)	I_{sc} (A)	m (kg)	IP
430	22,02	33,49	12,84	40,3	13,3	26	68

Furthermore, the nominal data of the three-phase inverter type SE16 *[17]* from the SolarEdge manufacturer used in this paper are presented in Table 2.

Table 2: *Nominal data of the three-phase inverter SE16*

P_N (kW)	U_N (V)	I_N (A)	EFF (%)	m (kg)	IP
16	400	25,5	97,7	33,2	65

2.2   Simulation model of a flat roof

For the calculation of electricity production in this paper, a flat roof with dimensions of 52 x 52 metres was used for the simulation model. With the solar modules orientated to the south, 26 solar modules were placed in each row. In Fig. 2 there is a model of the south-orientated solar modules, which are tilted for angle β relative to the flat roof and apart by a distance *d*. In the summertime the angle of incidence of the sun's rays is bigger than in the winter, causing less shading for each subsequent row due to the first. In winter there is evidently a lot more shading present, except for the first row. To conclude, it is evident from Fig. 2 that the greater the distance *d*, the less shading there is, but, at the same time, less modules can be placed on the roof.
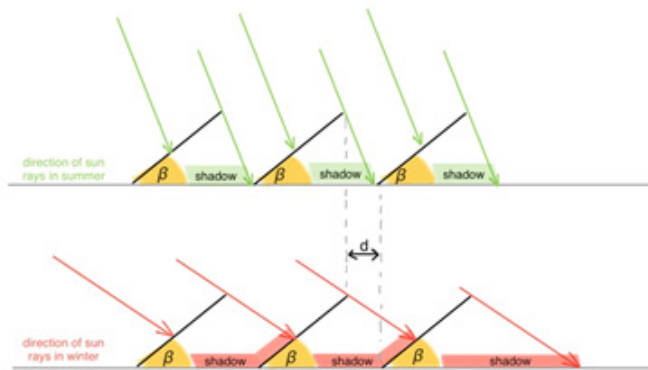
Figure 2: *South orientation of solar power plant modules with the influence of shadowing [18]*

For East-West orientation 2 x 26 modules were placed in each column inside the simulation model, according to Fig. 3. In the simulation model it was investigated how the distance and slope of the solar modules affected the mutual shading of the solar modules.
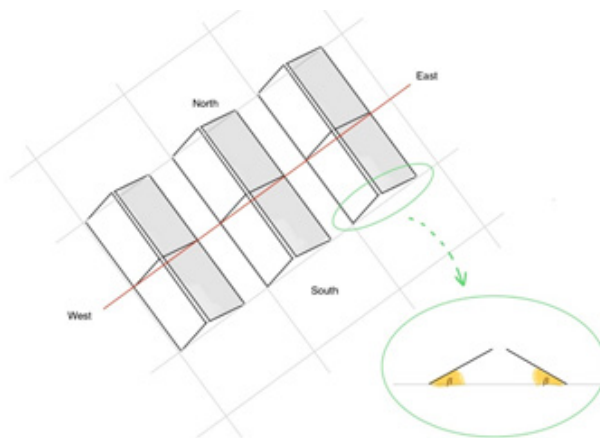
Figure 3: *East-West orientation of solar power plant modules – concept for a flat roof [18]*

3   RESULTS

3.1   South orientation of solar modules on a flat roof

When analysing the placement of south-oriented solar modules on a flat roof, it is necessary to consider the geographical latitude and longitude where the roof with the solar power plant is located. The geographical latitude affects the optimal tilt of the solar modules, at which the power plant produces the maximum amount of electricity annually. The electricity production results for the first row of 26 south-oriented solar modules at different tilt angles are presented in Table 3. The red cells represent at which tilt angle of the modules β the production is the lowest for each month. On the contrary, the green cells show the highest production at a certain tilt angle of the modules. It is evident that, in the winter months, a, bigger tilt is optimal, whereas, in the summer, there is more production with a smaller tilt.

Table 3: *Electricity production W in MWh for different tilt angles and months for the first row*

β (°)	W_{jan}	W_{feb}	W_{mar}	W_{apr}	W_{may}	W_{jun}	W_{jul}	W_{aug}	W_{sep}	W_{oct}	W_{nov}	W_{dec}	W_{Σ}
3	0,38	0,58	0,95	1,38	1,66	1,73	1,82	1,46	1,16	0,74	0,41	0,31	**12,57**
10	0,46	0,67	1,03	1,44	1,69	1,74	1,85	1,51	1,25	0,83	0,48	0,38	**13,33**
20	0,56	0,79	1,12	1,50	1,70	1,73	1,85	1,55	1,34	0,94	0,57	0,47	**14,12**
30	0,64	0,89	1,18	1,53	1,67	1,68	1,81	1,55	1,40	1,02	0,64	0,54	**14,55**
40	0,71	0,96	1,21	1,51	1,60	1,60	1,73	1,52	1,42	1,08	0,69	0,60	**14,63**
50	0,75	1,00	1,21	1,47	1,50	1,48	1,61	1,45	1,40	1,10	0,73	0,64	**14,33**
60	0,77	1,02	1,18	1,38	1,37	1,33	1,46	1,35	1,36	1,10	0,74	0,66	**13,72**
70	0,78	1,01	1,12	1,26	1,20	1,14	1,27	1,21	1,27	1,07	0,74	0,66	**12,72**

Fig. 4 shows the dependence of annual production on the tilt of the modules for the first row of 26 south-oriented solar modules.

The simulation results show in Fig. 4, that the optimal tilt angle for the location of Lenart city in Slovenia (46.5834° N and 15.8262° E) is 38,5° for maximum annual electricity production of a solar power plant. In the installation of the power plant, the rows are spaced apart by a distance *d* based on the tilt angle, as shown in Fig. 2, where the shading must be considered of the previous row of modules on the next. Table 4 presents the electricity production results of the second row of solar modules compared to the first row for different distances *d* between the rows at a tilt angle of 38,5°. The production of the blue cells of the shaded row of modules is less than 10 percent lower than that of the unshaded 1st row of modules with southern orientation (the green cells in Table 4).

Fig. 4 shows the dependence of annual production on the tilt of the modules for the first row of 26 south-oriented solar modules.
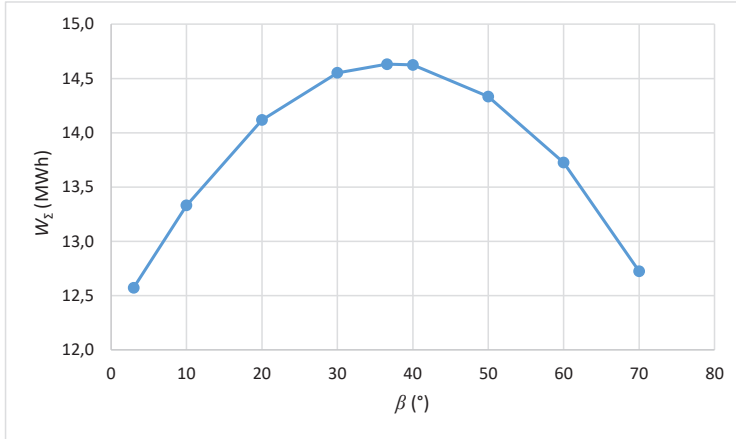
Figure 4: Annual electricity production W_Σ in dependency of tilt angle β for the first row

Table 4: *Electricity production W (MWh) for different distances between the 1ˢᵗ row and 2ⁿᵈ shaded row, with 26 solar modules in the 2ⁿᵈ row at a tilt angle of 38,5°*

d (cm)	W_{jan}	W_{feb}	W_{mar}	W_{apr}	W_{may}	W_{jun}	W_{jul}	W_{aug}	W_{sep}	W_{oct}	W_{nov}	W_{dec}	W_Σ
0	0,21	0,29	0,44	0,84	0,98	0,98	1,07	0,87	0,57	0,37	0,23	0,19	**7,01**
10	0,23	0,31	0,59	0,89	1,04	1,08	1,13	0,92	0,77	0,38	0,25	0,20	**7,77**
30	0,24	0,36	0,74	1,00	1,39	1,46	1,55	1,12	0,86	0,52	0,26	0,22	**9,71**
50	0,25	0,50	0,78	1,37	1,49	1,50	1,61	1,40	1,00	0,65	0,32	0,23	**11,07**
70	0,32	0,57	0,97	1,41	1,51	1,52	1,64	1,43	1,28	0,68	0,38	0,24	**11,92**
90	0,39	0,60	1,11	1,43	1,53	1,54	1,66	1,44	1,34	0,80	0,42	0,32	**12,54**
110	0,42	0,73	1,14	1,45	1,55	1,55	1,67	1,46	1,35	0,94	0,45	0,36	**13,05**
130	0,45	0,83	1,15	1,45	1,56	1,56	1,68	1,47	1,36	0,99	0,51	0,37	**13,35**
150	0,49	0,92	1,16	1,47	1,57	1,57	1,70	1,48	1,37	1,01	0,56	0,37	**13,64**
1ˢᵗrow	0,69	0,94	1,20	1,52	1,63	1,64	1,76	1,53	1,41	1,06	0,68	0,58	**14,63**

Fig. 5 shows the normalised electricity production of the 2nd shaded row relative to the 1st unshaded row for different distances between both rows. The purple portion of the surface curves on the 3D graph is useful for adequate production at a solar module tilt of 38.5°. The annual electricity production with a 90 cm distance between the shaded rows is 14.3 percent lower compared to the production of the first unshaded row. At 30 cm, the electricity production of the shaded row is 33.6 percent lower.
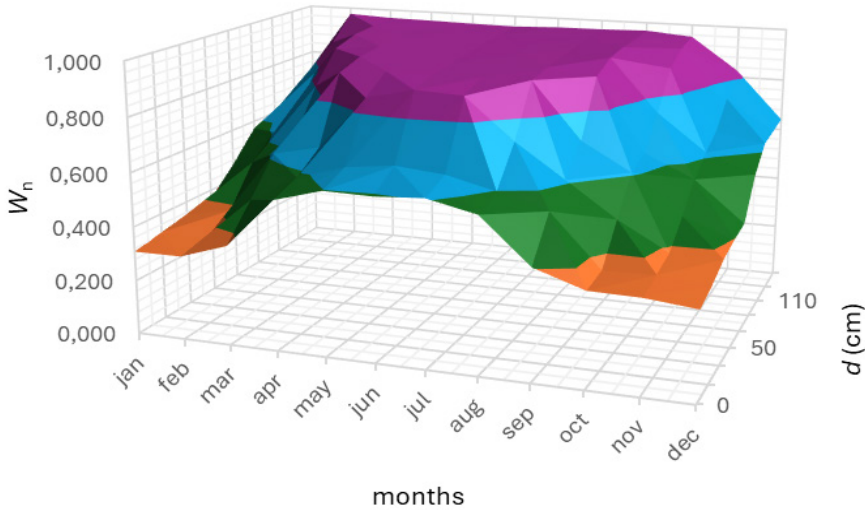
Figure 5: *Electricity production of the 2nd shaded row normalised to the production of the 1st row at a tilt angle of 38,5°*

3.2   East-West orientation of solar modules on a flat-roof

When analysing the installation of East-West oriented solar modules on a flat roof, it is not necessary to consider the geographical latitude and longitude where the roof with the solar power plant is located. The tilt angle of the solar modules relative to the flat roof in an East-West orientation does not affect electricity production significantly. The electricity production results for 26 east-oriented and 26 west-oriented solar modules (2x26 solar modules included in each column, as shown in Fig. 3) at different tilt angles β are presented in Table 5. Due to self-cleaning of the solar modules during rain and the sliding of snow in the winter, an angle β between 12 and 15 degrees is recommended.

Table 5: *Electricity production W (MWh) for different tilt angles and months for an East-West orientation*

β (°)	W_{jan}	W_{feb}	W_{mar}	W_{apr}	W_{may}	W_{jun}	W_{jul}	W_{aug}	W_{sep}	W_{oct}	W_{nov}	W_{dec}	W_{Σ}
3	0,68	1,07	1,82	2,70	3,29	3,43	3,62	2,87	2,24	1,39	0,76	0,55	**24,43**
7	0,69	1,08	1,82	2,70	3,28	3,42	3,61	2,87	2,24	1,40	0,76	0,56	**24,43**
11	0,69	1,08	1,82	2,69	3,27	3,41	3,60	2,86	2,24	1,40	0,76	0,56	**24,39**
15	0,69	1,08	1,81	2,68	3,24	3,39	3,58	2,84	2,23	1,40	0,77	0,56	**24,27**
19	0,70	1,09	1,81	2,67	3,21	3,36	3,55	2,83	2,22	1,39	0,77	0,56	**24,16**
23	0,70	1,09	1,80	2,65	3,18	3,33	3,52	2,80	2,21	1,39	0,77	0,57	**24,00**
27	0,70	1,09	1,78	2,62	3,13	3,28	3,47	2,77	2,19	1,38	0,77	0,57	**23,75**
31	0,70	1,09	1,77	2,59	3,09	3,23	3,42	2,74	2,17	1,37	0,76	0,57	**23,50**
35	0,70	1,08	1,75	2,56	3,04	3,19	3,37	2,70	2,15	1,36	0,76	0,57	**23,22**
39	0,69	1,08	1,73	2,53	2,98	3,13	3,31	2,66	2,12	1,35	0,75	0,56	**22,90**
43	0,69	1,07	1,70	2,48	2,92	3,07	3,26	2,61	2,09	1,33	0,75	0,56	**22,52**

From Fig. 6 it is evident that, in the colder months of the year (January, February, November and December), the tilt angle of the solar modules in the East-West orientation practically does not affect the electricity production. The influence of the tilt angle is more pronounced during the warmer months (May, June, July and August). The question remains as to what happens when additional columns of solar modules are added to the first column in the East-West orientation on a flat roof. Is there mutual shading between the columns in that case? Practically not, because the height of the solar module junctions in one column is fairly low, as shown in Fig. 7, and it affects neighbouring columns minimally according to the electricity production calculations at different spacings between the columns (presented in Table 6).
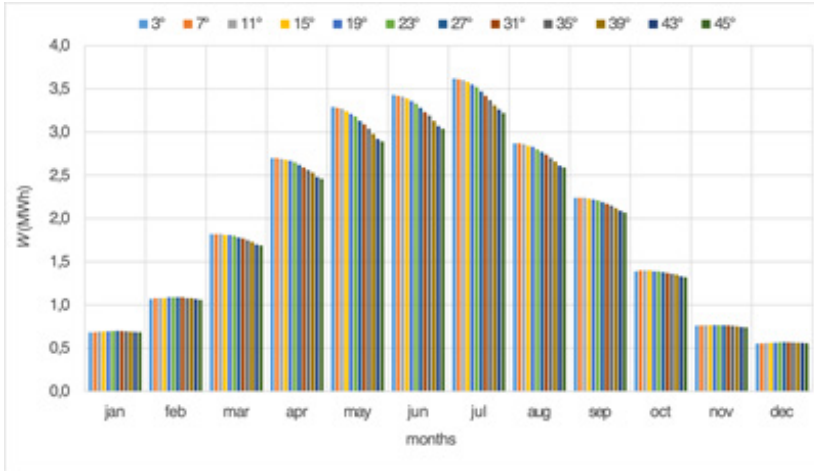
Figure 6: *Electricity production of East-West orientation for different tilt angles and months*

In Fig. 7, there is an example of east-west orientated solar modules used in practice.

Figure 7: *Practical placement of East-West oriented solar modules (own photo)*

In Table 6 the results of the annual electricity production calculations show that the impact of the distance between columns in the East-West orientation due to shading is negligible. The blue cells indicate a decrease in electricity production of less than 1 percent compared to the unshaded column, and the ochre cells indicate a decrease of less than 2 percent. In all other white cells, the electricity production of the shaded columns is less than 4 percent lower compared to the unshaded column. Therefore, in practice, spacings of 25 to 50 cm are used, primarily for maintenance and servicing of the solar power plant.

Table 6: *Electricity production W (MWh) for different distances between the 1st column and 2nd column for 2x26 solar modules in an East-West orientation for a tilt angle of of 15°*

d (cm)	W_{jan}	W_{feb}	W_{mar}	W_{apr}	W_{may}	W_{jun}	W_{jul}	W_{aug}	W_{sep}	W_{oct}	W_{nov}	W_{dec}	W_{Σ}
0	0,67	1,05	1,77	2,63	3,19	3,32	3,51	2,80	2,18	1,35	0,74	0,54	**23,75**
10	0,68	1,05	1,77	2,63	3,19	3,33	3,51	2,80	2,19	1,35	0,75	0,55	**23,78**
30	0,68	1,07	1,78	2,64	3,20	3,33	3,52	2,80	2,19	1,37	0,75	0,55	**23,86**
50	0,68	1,07	1,79	2,66	3,22	3,37	3,56	2,82	2,21	1,38	0,75	0,55	**24,05**
70	0,68	1,07	1,80	2,66	3,22	3,37	3,56	2,82	2,22	1,38	0,76	0,55	**24,09**
90	0,68	1,07	1,80	2,67	3,23	3,38	3,56	2,83	2,22	1,38	0,76	0,55	**24,11**
110	0,69	1,07	1,80	2,67	3,23	3,38	3,57	2,83	2,22	1,38	0,76	0,56	**24,13**
130	0,69	1,07	1,80	2,67	3,23	3,38	3,57	2,83	2,22	1,38	0,76	0,56	**24,16**
150	0,69	1,08	1,81	2,67	3,23	3,38	3,57	2,83	2,22	1,39	0,76	0,56	**24,19**
1st col.	0,69	1,08	1,81	2,68	3,24	3,39	3,58	2,84	2,23	1,40	0,77	0,56	**24,27**

4   ANALYSIS

For the simulation model presented in Section 2.1, the simulation calculations of electricity production were performed for both possible configurations (South orientation and East-West orientation, as shown in Fig. 8) of the solar power plant on the flat roof discussed in the paper.

(a)   (b)
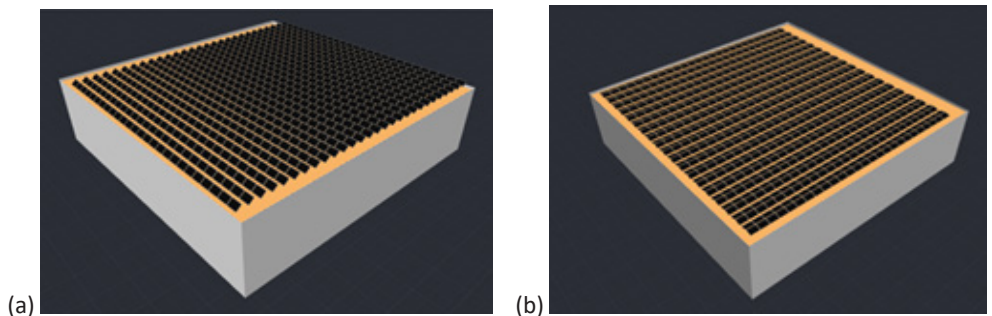
Figure 8: *Simulation model in SolarEdge Designer software; (a) South orientation and (b) East-West orientation.*

In Table 7 there are the calculations` results for a simulation model with dimensions 50x50, in which case the flat roof has 2500 m² of useful area for solar modules` installation. What is important to consider is the fact that, in practice, not all the area of the flat roof is used for solar modules` placement, because there should be space left for service and maintenance access to

solar modules, as well as enough place for ensuring fire safety *[19]*. In Table 7 P_i represents the installed peak power of the solar modules, W_{Σ} is the annual electricity production, *WD* is the energy density in terms of annual electricity production per flat-roof surface, *PI* is the performance index in terms of annual electricity production per installed solar modules peak power, and *PD* is the power density in terms of the installed peak power of solar modules per flat-roof surface. From the results of the calculations presented, it is evident that the best configuration is East-West, because it has far higher values for all the variables listed above. It is especially important to emphasise annual energy production W_{Σ}, which, in the East-West orientation is 23,78% higher than in the south orientation at just 7,64% higher power density in terms of the installed peak power of solar modules per flat-roof surface *PD*.

Table 7: *Electricity production for different orientation, distance and tilt angle – simulation model*

Orientation	*d* (cm)	*β* (°)	*No. of modules*	P_i (kW$_p$)	W_{Σ} (MWh)	*WD* (kWh/m^2)	*PI* (Wh/W$_p$)	*PD* (kW$_p$/m^2)
South	90	38,5	728	313,04	181,31	72,524	579	0,125
South	30	15	910	391,30	348,20	139,28	890	0,157
East-West	30	15	988	424,84	456,82	186,33	1075	0,170

5   DISCUSSION

The research about solar power plant configuration on a flat roof for the highest annual production of electric energy is presented in this article. When placing solar modules on a flat roof at a certain tilt shading occurs, as a problem which should be considered while determining the best configuration. The data show that the optimal tilt angle for Lenart in Slovenia, where the simulation model was located, is 38,5°. However, in practice, it shows up that, at this tilt of solar modules on a flat roof, the annual production is actually the lowest compared to the south and East-West orientation, both at a tilt angle of 15°. The calculations show that it is possible to provide a power density of 0,170 kW$_p$/m^2 on a flat roof with East-West orientation of the solar modules. This means that we can install 170 W of solar module power per square metre, which produces 186.33 kWh per square metre of flat roof annually.

6   CONCLUSIONS

The green transition of a sustainably oriented society requires the use of renewable resources. Direct use of solar energy is possible with solar power plants, whose installed capacity is increasing rapidly worldwide. In exploiting solar energy, power plants are installed on structures of various sizes and roof topologies. A particular challenge is the installation of a solar power plants on flat roofs, where it turns out that the placement of south-facing modules does not contribute to maximum electricity production. Therefore, this article presents methods and procedures for determining the optimal placement of solar modules on a flat roof of a building to

achieve maximum annual production. Commercial software tools were used for the production calculations, which can determine the appropriate configuration of the module layout for maximum production. It turned out that the East-West orientation of the solar modules is the best for a flat roof. One of the advantages of East-West orientation is higher power density, which results in increased electricity production. This is a good solution, because it is more common for buildings to be space-constrained than not. Furthermore, the East-West orientation is the most aerodynamic out of all configurations, which is especially beneficial for flat roofs in windy areas. Because East-West systems are tilted with an angle of 15°, self-cleaning capabilities are increased, which is, again, important for the maximisation of electricity production. Another great thing about this orientation is that the solar modules are installed back-to-back, which reduces the risk of shading, and therefore increases the efficiency of the solar power plant.

References

[1]   **D. H. Meadows et al.:** *The Limits to Growth*, Universe Books, 1972

[2]   **Directorate-General for Structural Reform Support:** *Technical support for implementing the European Green Deal*, Publication Office of the European Union in Luxembourg, 2020

[3]   **M. Borowiecki et al.:** *Accelerating the EU's green transition*, OECD Economics Department Working Papers, No. 1777, 2023

[4]   **A. M. Reveshti et al.:** I*nvestigating the effect of new and old weather data on the energy consumption of buildings affected by global warming in different climates*, International Journal of Thermofluids, No. 19, 2023

[5]   **A. A. Ahmed:** *Global warming potential, water footprint, and energy demand of shared autonomous electric vehicles incorporating circular economy practices*, Sustainable Production and Consumption, No. 36, 2023

[6]   **Editorial:** *Sustainable development of energy, water and environment systems in the critical decade for climate action*, Energy Conversion and Managementle, No. 296, 2023

[7]   **P. Jain et al.:** *Agrovoltaics: Step towards sustainable energy-food combination*, Bioresource Technology Reports, No. 15, 2021

[8]   **C. J. Torrente et al.:** *Simulation model to analyze the spatial distribution of solar radiation in agrivoltaic Mediterranean greenhouses and its effect on crop water needs*, Applied Energy, No. 353, 2024

[9]   **International Code Council:** *International Building Code*, USA, 2021

[10]   **Kastelec et al.**: Sončna energija v Sloveniji, Ljubljana, 2007

[11]   **E. Golubovska et al.:** *Analytical estimation of the optimal PV panel tilt based on a clear sky irradiance model*, Journal of Energy Technology, Vol. 16, Iss. 4, 2023

[12]   **S. Seme:** *Optimalno sledenje fotonapetostnega sistema soncu ob upoštevanju izgub pogonskega sklopa*, doctoral dissertation, UM FERI, 2011

[13]   **Solarific.** Available: https://solarific.co/si (date of last access: 13. 8. 2024)

[14]   **A. Dudek:** *Equity research: SolarEdge Technologies, INC.*, University of Algarve, 2023

[15]   **Energy Simulation Validation:** *SolarEdge Designer Review*, 2019. Available: https://knowledge-center.solaredge.com/sites/kc/files/se-designer-simulation-validation-dnv-gl-report.pdf (last access: 13. 8. 2024)

[16]   **Huasun.** Available: G10-182-108-DS_EN (huasunsolar.com) (last access: 13. 8. 2024)

[17]   **Huason.** Available: se-three-phase-inverter-extended-power-datasheet.pdf (solaredge.com) (last access 13. 8. 2024)

[18]   [**Y. Yang et al.:** *Potential analysis of roof-mounted solar photovoltaics in Sweden*, Applied Energy, No. 279, 2020

[19]   **SolarPower Europe:** *Rooftop PV Fire Safety Factsheet*. Available: https://api.solarpowereurope.org/uploads/Factsheet_Rooftop_PV_Fire_Safety_vfinal_33eaab8bb3.pdf?updated_at=2024-03-18T15:38:06.684Z (last access: 13. 8. 2024)

Nomenclature

α	Incident angle of the sun's rays
h	Hour angle
δ	Declination
L	Longitude
P_{max}	Maximum power of the solar module
EFF	Efficiency of the solar module
U_{mp}	Optimum operating voltage
I_{mp}	Optimum operating current
V_{oc}	Open circuit voltage
I_{sc}	Short circuit current
m	Solar module mass
IP	Ingress protection
β	Tilt angle of the modules relative to the flat roof
d	Distance between the modules
P_i	Installed peak power of the solar modules
W_Σ	Annual electricity production

WD	Energy density of the annual electricity production per flat-roof surface
PI	Performance index of the annual electricity production per installed solar module`s peak power
PD	Power density in terms of the installed peak power of the solar modules per flat-roof surface

Journal of
Energy
Technology

HARDWARE IN THE LOOP TESTING OF A PROTECTION MONITORING AND DIAGNOSTIC SYSTEM

PREIZKUŠANJE STROJNE OPREME V ZANKI SISTEMA ZA NADZOR IN DIAGNOSTIKO ZAŠČITE

Jernej Černelič[R,], Boštjan Polajžer[1], Janez Zakonjšek [2], Alexey Nebera[3], Gorazd Hrovat[4]

Abstract

Protection, automation, and control (PAC) devices are very important for the reliable operation of electric power systems (EPS), which can be improved further by monitoring the PAC devices. One way is to apply a protection monitoring and diagnostic (PMD) system, which was tested using a real-time digital simulator and two numerical protection relays in the hardware in the loop configuration. Furthermore, the communication between the protection relays and the PMD system was also tested, while the EPS faults were simulated in a safe environment on a digital simulator in real-time. When a fault occurs in the EPS, the PMD system performs the fault analysis, and generates a disturbance report within several minutes after the fault. The tested PMD system also gathers all protection relays' settings, thus reducing the workload of protection specialists significantly.

[R]   Corresponding author: Dr, Jernej Černelič, University of Maribor, Faculty of Electrical Engineering and Computer Science, Koroška Cesta 46, 2000 Maribor, Tel.: +386 2 220 7340, E-mail address: jernej.cernelic@um.si

[1]   University of Maribor, Faculty of Electrical Engineering and Computer Science, Maribor, Slovenia

[2]   Relarte d.o.o, Bohinjska Bistrica, Slovenija

[3]   Kontron d.o.o., Kranj, Slovenija

[4]   ELES d.o.o., Ljubljana, Slovenija

Povzetek

Naprave za zaščito, avtomatizacijo in nadzor so zelo pomembne za zanesljivo obratovanje elektroenergetskega sistema (EES), kar lahko dodatno izboljšamo z uporabo sistemov za nadzor teh naprav. Eden od način je uporaba sistema za nadzor in diagnostiko zaščite, ki je bil preizkušen s pomočjo digitalnega simulatorja v realnem času in dveh digitalnih zaščitnih relejev, povezanih s simulatorjem v zaprti zanki. Preizkušene so bile tudi komunikacijske povezave med zaščitnimi releji in sistemom za nadzor in diagnostiko, pri čemer so bile okvare v EES simulirane v varnem okolju, tj. na digitalnem simulatorju v realnem času. Kadar pride do okvare v EES, sistem za nadzor in diagnostiko opravi analizo okvare in izdela poročilo že v nekaj minutah po okvari. Poleg tega preizkušen sistem za nadzor in diagnostiko zaščite zbere vse nastavitve vseh zaščitnih relejev in tako zmanjša delovne obremenitve specialistov za zaščito.

1   INTRODUCTION

The reliability of Electric Power Systems (EPS) depends on protection, automation, and control (PAC) devices [1,2]. In North American EPS, for example, the rate of protection device misoperation is between 6 % and 7 %, according to the North American Electric Reliability Corporation (NERC) [3]. Around 32 % of all misoperations are caused by incorrect settings, logic, or other protection design errors. Around 18 % of all misoperations are caused by protection device malfunctions, and around 10 % of all misoperations are caused by communication failures. These misoperations add up to around 60 % of all protection device misoperations. Most protection device malfunctions are detected after the fault events are analyzed, or after preventive maintenance.

The malfunctions of the protection device have a high impact on the reliable operation of EPS, because some malfunctions may lead to a wider spread of an initially local EPS disturbance [2]. The protection device malfunctions are often called "hidden failures", as they may remain undetected until a short circuit or other disturbance occurs [4-7]. Hidden failures represent themselves when the protection device fails to clear the fault in the protected element (dependability), or when the protection device operates without a fault, or operates non-selectively with a fault outside the protected zone (security) [5]. All protection device malfunctions can be subdivided into three main categories: protection device failures, configuration errors, and external failures (Figure 1). The protection device failure can be caused either by hardware or software failure. The hardware failures include failures in the power supply, discrete input/output boards, the main board (CPU and memory), measurement boards, and communications. The software failures can be subdivided into firmware failure, Continuous Function Chart (CFC) logic failure, and manufacturer-specific software failure. The external failures can be subdivided into a current transformer (CT), voltage transformer (VT), and other secondary circuit failures, operational supply circuit failures, communication channels failures, and circuit breaker (CB) control circuit failures.

With such a high number and diversity of failures, there is a strong need for a protection monitoring and diagnostic (PMD) system to identify all these failures [8]. Modern PAC devices provide information about their software, hardware settings, and statuses. Moreover, some PAC devices can also provide information about the conditions of external circuits. However, because of the high number of PAC devices and the diversity of information between different software versions and device types, it is already very challenging to gather all settings, statuses, and other information in one system.
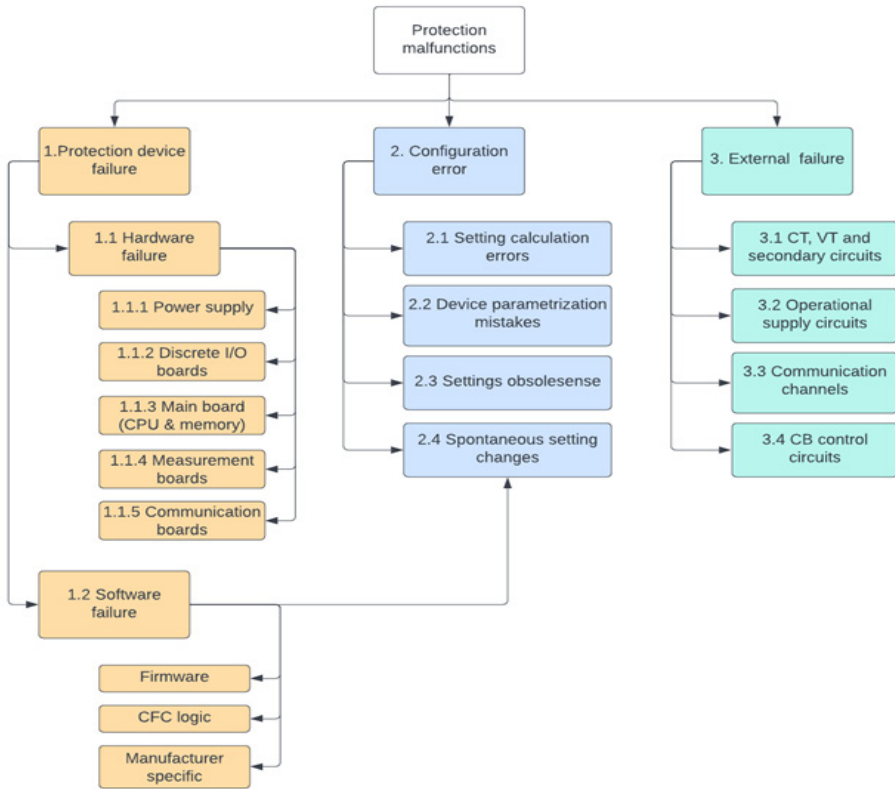
Figure 1: *Structure protection malfunction causes*

Despite all the challenges, an even more complex system, such as a wide-area monitoring, protection, and control (WAMPAC) system, is proposed, to minimize the incorrect operations of all PAC devices, and, consequently, improve the reliability of EPS [1,9,10]. The WAMPAC system is expected to become an indispensable part of EPSs with a high level of operational uncertainties. One of the key functions of the WAMPAC system is the PMD system.

The most successful implementation of such new technologies in an EPS is achieved by real-time testing in a closed-loop manner using an appropriate Real-Time Digital Simulator (RTDS). This means that the operation of the devices under test (in our case, the PMD system) feeds back to the states of the EPS model. Such tests are referred to as Controller Hardware-In-the-Loop (C-HIL) tests. The assessment of different HIL approaches for WAMPAC testing is provided in [11], with the focus on phasor measurement unit implementation in the HIL tests. In [12] the RTDS was used to test the implementation of a protection device and self-healing function in the simulated microgrid environment. In [13] the IEC 61850 generic object-oriented substation event (GOOSE) protocol was used to test the centralized microgrid controller in transition between the island and grid-connected operating mode using the C-HIL configuration. The HIL tests are used widely to validate the performance of PAC devices used in microgrids, AC and HVDC transmission systems [14-18].

In this paper, the PMD system, developed by the Kontron company, is presented in Chapter 2, and the hardware in the loop test setup is described in Chapter 3. The test results are collected and explained in Chapter 4, while Chapter 5 summarizes the paper and gives conclusions.

2   PROTECTION MONITORING AND DIAGNOSTIC SYSTEM

The PMD system requires information about the EPS topology and EPS equipment status, which can be obtained using the common information model form Network Model Management or SCADA/EMS system [19,20]. The EPS equipment status signals are collected from the Supervisory Control And Data Acquisition (SCADA) system, while the EPS topology is obtained from the EPS model. The SCADA status signals contain information about the status of the PAC devices, and the 'in service' or 'out of service' information about power lines, control switches, and other primary EPS equipment.

When the disturbance occurs, the PMD systems collect the disturbance records and configuration files automatically from all the protection devices, i.e., those that only detected the disturbance and those that operated (tripped). The disturbance records can also be uploaded to the PMD system manually. The measured voltage and current signals are then retrieved from the disturbance records, checked for feasibility to evaluate their reliability, and filtered automatically, identifying only those with short-circuit current or transient patterns.

Next, the PMD system synchronizes the time of received voltage and current signals automatically, because the signals are measured on different devices and might not have synchronized clocks. Additionally, the measurements are often obtained, not only from different devices, but also from different power facilities. The proposed time synchronization method ensures high synchronization accuracy to a common time scale, with the worst-case error of less than 0.1 ms within one power facility, and less than 1 ms between different power facilities.

After automatic synchronization, the PMD system identifies the start and end times of the disturbance. The start moment is considered a transient moment, registered by the recorded voltage and current signals, while the end moment is the moment of clearing the disturbance. Consequently, the total fault clearing time can be obtained from the start and end time of the disturbance. Then, the PMD system calculates the RMS values of the pre-fault and fault currents and voltages. The fault type and phase selection algorithms are initiated next, identifying the type of fault and affected phases. If a fault is located on a power line, the fault location algorithm [21] is initiated, but, if the PMD system fails to identify the fault type and location automatically, then it must be identified manually by the protection specialist.

Furthermore, the PMD system creates the disturbance reports automatically, based on the abovementioned disturbance records and analysis process. The content of the disturbance report is presented in Figure 5 in Chapter 4 for a selected example.

3   HARDWARE IN THE LOOP TESTING

The discussed PMD system was tested using the C-HIL configuration with the RTDS, which allows to test the measurement and PAC devices even in transient conditions. Moreover, the effect of PAC devices on the EPS can be analyzed without any hazard to the stability of the real EPS. Figure 2 details the entire test setup for testing the discussed PDM system.

A single fully licensed NovaCor RTDS chassis can calculate up to 600 single-phase network nodes using a simulation step of 25 to 50 μs. It consists of 10 IBM Power8 RISC 3.5GHz licensed cores, 12 analog input channels with 16-bit resolution, ±10 V range and a 1 MS/s sampling rate, 24 analog output channels with 16-bit resolution and a ±10 V range and 160 kS/s sampling rate, and up to 64 digital input or output channels. The NovaCor RTDS also consists of an FPGA unit, which allows parallel simulation of subnetworks with power electronic devices such as FACTS that require shorter simulation steps of 1 to 5 μs.
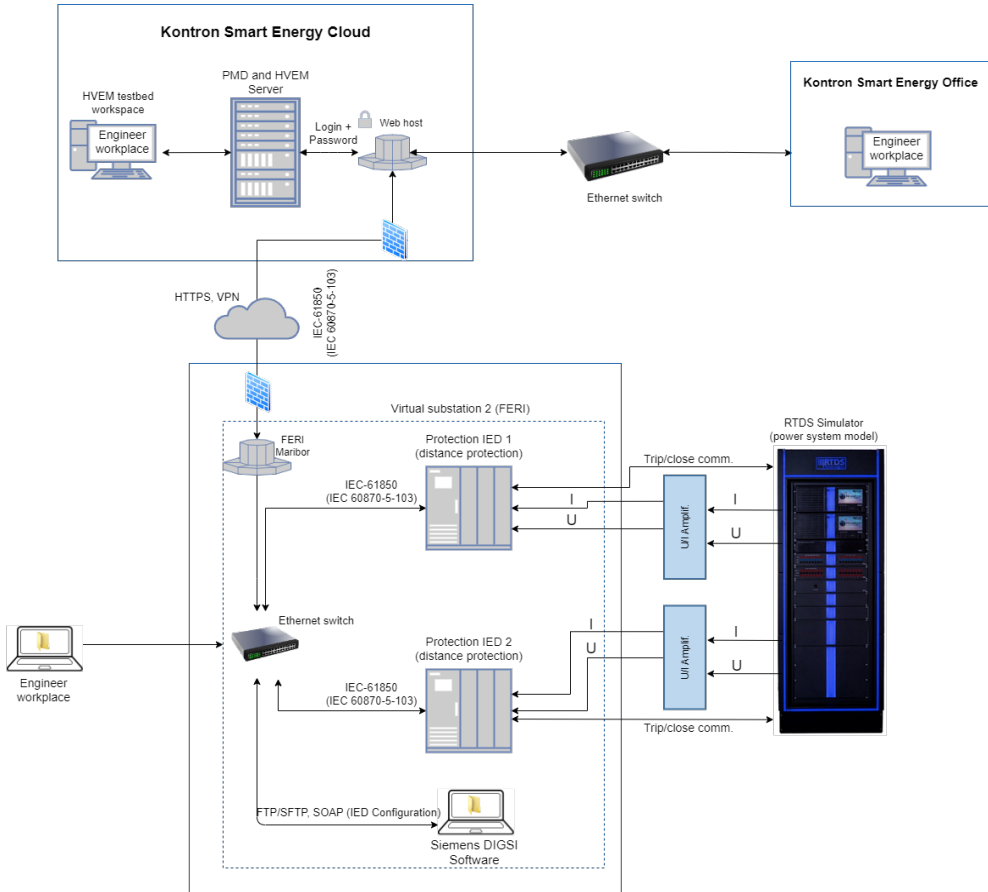
Figure 2: *Hardware in the loop test setup*

The hardware in the loop test setup consists of an RTDS system, two voltage and current amplifiers, two numerical protection relays, and a remote connection to the PMD system (Figure 2). The PMD system, running on a server in a remote location of the Kontron company, was connected to two Siemens Siprotec 7SD5 numerical protection relays using a network switch with a Virtual Private Network (VPN) connection. The RTDS was used to simulate faults on a power line model, using a simulation step size of 50 μs. The calculated voltages and currents captured on the discussed power line were realized on the RTDS analog output channels. Two voltage and current amplifiers were used to amplify the voltages and currents to a specified range

of 7SD5 protection relays. The trip signals of the 7SD5 protection relays were connected back to the digital input channels of the RTDS, where the signals were used to operate the corresponding circuit breakers in the power line model. Consequently, the faulted power line model can be disconnected from the rest of the EPS in real time, and the correctness of the protection relay operation can be studied.

3.1   Simulation model

The simulated model of the EPS (Figure 3) consisted of a single 220 kV three-phase power line between the substations Podlog (Slovenia) and Obersielach (Austria). The power line model was divided into two sections, with the fault model in between, allowing the user to change the fault location with the parameter *dL*. Additionally, it was possible to select any combination of faulted phases with or without ground connection, and, consequently, simulate the single-phase, two-phase, or three-phase faults. The model also consisted of circuit breakers operated by the protection relays in case of a fault, while the VTs and CTs were considered only by the constant ratio. The substations were modeled using corresponding equivalent impedances and power sources. The RLC load was also added, to set the power flow for normal operation.
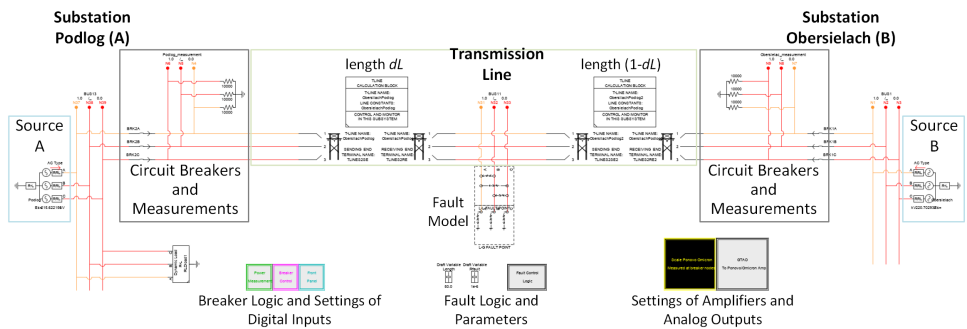

Figure 3: Electric power system model

The parameters of the symmetrical components of the modeled power line are collected in Table 1, where *L* is the length of the line, R_p, X_p and C_p are the resistance, reactance, and capacitance of the positive sequence, respectively, while R_0, X_0, and C_0 are the resistance, reactance, and capacitance of the zero sequence. Additionally, I_{max} is the maximum steady-state current.

Table 1: Podlog – Obersielach power line parameters

L [km]	R_p [Ω]	X_p [Ω]	C_p [μF]	R_0 [Ω]	X_0 [Ω]	C_0 [μF]	I_{max} [A]
65.492	3.980	27.029	0.582	14.017	66.296	0.372	920

3.2   Distance protection relays

Two numerical distance protection relays, Siemens Siprotec 7SD5, were used to test the PMD system. First, the VPN connection was tested when the PMD system collected the settings from the 7SD5 relays. The most important settings of distance protection are collected in Table 2, where R_{LL} and X_{LL} are the primary resistance and reactance settings for the line-line faults, while

R_{LE} and X_{LE} are the primary resistance and reactance settings for the line-earth faults. Protection zones 1-3 are directed towards the line, while the 4th zone is undirectioned.

Table 2: *Distance protection zone settings*

Substation	Zone	R_{LL} [Ω]	R_{LE} [Ω]	X_{LL} & X_{LE} [Ω]	Delay [s]
Podlog (Side A)	1	22.97	45.95	22.97	0
	2	32.4	64.87	32.4	0.75
	3	76.7	85	76.7	2
	4	85	85	85	4.8
Obersielach (Side B)	1	22.97	45.95	22.97	0
	2	35.14	70.28	35.14	0.4
	3	92.46	96	92.46	1.35
	4	96	96	96	3

The 1st zone of distance protection is usually not delayed, and does not protect the entire power line, but only 85 % of the power line, while the 2nd zone protects the rest of the power line, but with a delay of 0.75 s for the Podlog location, or 0.4 s for the Obersielach location. Consequently, an unwanted delay in the relay protection operation occurs for the relay that detects the fault in the 2nd zone. Therefore, the protection relays are connected according to the Permissive Under-reaching Transfer Tripp (PUTT) communication scheme, which reduces the distance protection operation delays for these faults, i.e., when one of the protection relays detects a fault in the 1st zone, while the other relay detects a fault in the 2nd zone.

4   RESULTS

Ten tests were performed to test the discussed PMD system. The first eight tests were short circuit tests, where the parameters of the short circuit are presented in Table 3. The last two tests were diagnostic tests, where the VT fault was simulated by unplugging one of the voltage channels, and the protection relay restart was performed by unplugging the power supply. Both events were recorded by the PMD system, which notified the user.

Table 3: *PMD system tests*

No.	Fault type	dL [%]	φ_{UA} [°]	R_F [Ω]	T_F [s]
1.	ABC	50	90	0.1	0.2
2.	AG	50	75	10	0.2
3.	ABG	50	75	5/10	0.2
4.	BC	50	90	5	0.2
5.	BG	90	75	30	1.5
6.	CG	10	90	40	0.2
7.	BC	busbar P	90	10	0.6
8.	AB	busbar O	90	15	0.95

All the short circuit tests were performed at 75 % of the nominal power line loading before the short circuit occurred. The letters A, B, C, and G in Table 3 describe the fault type, where A, B, and C denote the phases of the three-phase system, and G denotes the ground connection. The dL parameter denotes the relative location of the fault on the power line, measured from the Podlog side. Note that the faults in test no. 7 and 8 were simulated on each busbar, not on the power line. The φ_{UA} parameter denotes the moment of short circuit occurrence in relation to the angle of voltage U_A. The R_F is the fault resistance, and T_F is the fault duration. In test no. 3, the two values of fault resistance are given, where the first fault resistance was between phases, and the second was the ground resistance.

Table 4 shows the absolute fault locations for both sides of the power line, denoted as dL_P for Podlog and dL_O for Obersielach. Comparison was made between the fault locations set in the simulation, reported by the relays, and calculated by the PMD system. The relays introduced significant errors in cases with high fault resistance, known as overreaching or underreaching. The error introduced by the PMD system was minimal, since the measurements from both sides of the power line were considered in the fault location calculation. In tests nos. 7 and 8, the PMD system correctly did not report the fault location, since the faults were on the busbar (behind the relay) and not on the power line. The last column shows the total fault clearing time T_{FC}, determined by the PMD system. Faults in tests nos. 5 and 6, which were in the second protection zone, were cleared in times shorter than the second zone delay, showing the advantage of the PUTT communication scheme. Additionally, the tests nos. 5 and 6 were performed with a relatively high value of fault resistance, R_F of 30 Ω and 40 Ω, respectively. Consequently, the protection relays determined the fault locations with a higher error than the PMD system. However, the fault location was determined less accurately by the protection relays, even at the fault resistance of 5 Ω in test no. 4. A detailed description of the results for test no. 1 is given in the next section, as well as the description of the time synchronization test.

Table 4: *PMD system test results*

No.	dL_P [km]			dL_O [km]			T_{FC} [ms]
	Set	Relay	PMD	Set	Relay	PMD	
1.	32.746	32.8	32.811	32.746	32.7	32.681	63
2.	32.746	35.8	32.811	32.746	31.8	32.681	72
3.	32.746	37.9	33.008	32.746	34.4	32.484	72
4.	32.746	34.6	32.615	32.746	31.9	32.877	55
5.	58.9428	59.5	58.943	6.5492	8.3	6.549	136
6.	6.5492	11	6.549	58.9428	52.4	58.943	82
7.	Busbar P	3.3	-	Busbar P	62.2	-	465
8.	Busbar O	205.8	-	Busbar O	-136.2	-	1131

4.1.   Test no. 1

The first test was the three-phase fault without ground connection (ABC). The fault duration was set as 0.2 s, and the fault location was in the middle of the modeled power line, while the fault resistance was 0.1 Ω. The fault was triggered at the phase angle of 90 ° of the phase voltage U_a. Figure 4.a) shows the simulated three-phase primary voltages and currents of the power line in substation Podlog obtained from the RTDS, while Figure 4.c) consists of the three-phase voltages and currents obtained from the secondary sides of the VTs and CTs in substation Podlog. Figure 4.b) and Figure 4.d) consist of the voltages and currents obtained from the Obersielach substation. The 7SD5 protection relays were supplied with the secondary voltages and currents presented in Figure 4.c) and Figure 4.d), respectively.
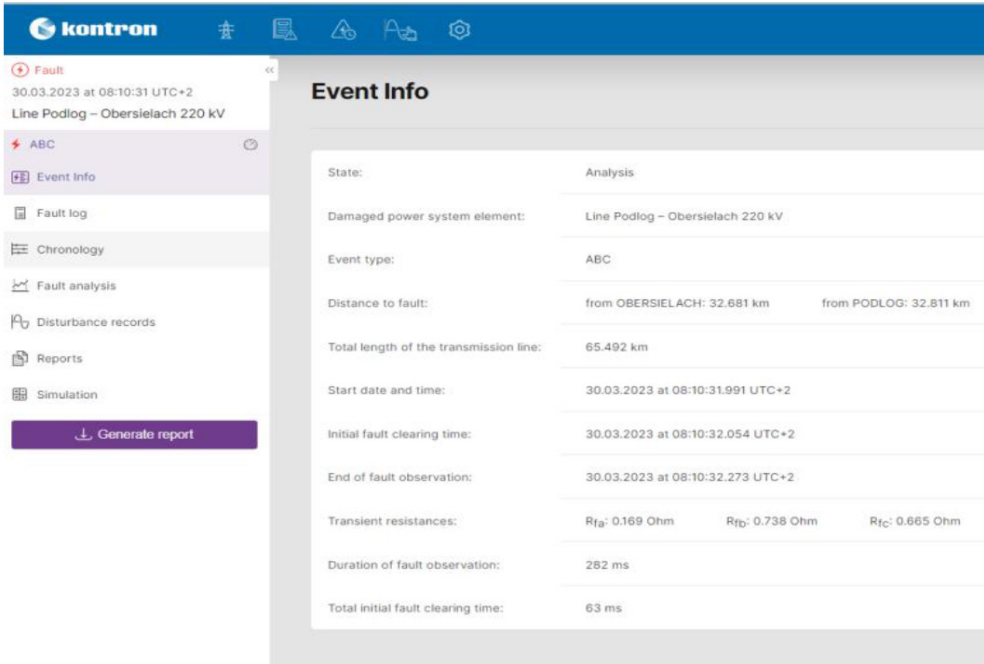
The PMD system collected the disturbance records from both protection relays within 2 minutes after the fault test was performed, and created the event report presented in Figure 5. The event report includes event info, log, chronology, fault analysis, disturbance records, reports, and simulation.
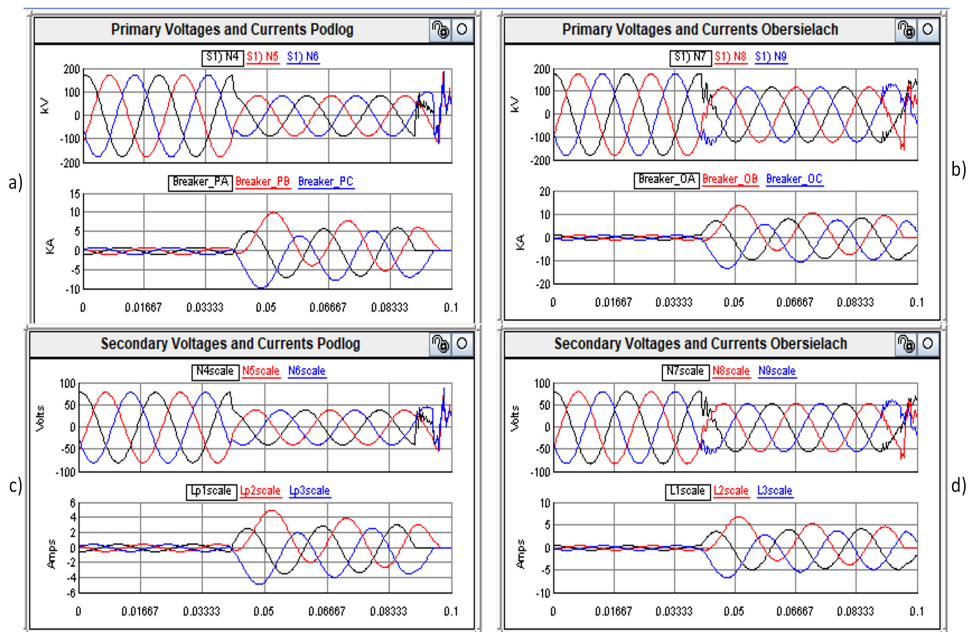
Figure 4: *Primary and secondary voltages and currents from RTDS*

The event info in Figure 5 presents very basic information, such as fault type, distance to fault, and fault clearing time of the event. The PMD system identified the fault type and distances from each end of the line to the fault successfully. The calculated fault distance from Podlog was 32.811 km, while the fault distance from Obersielach was 32.681 km. Since the actual middle of the line is 32.746 km, the identified fault locations are accurate to ±0.2 %. The PMD system also identified the transient fault resistances and the fault clearing time $T_{FC,}$ which, in this test, was 63 ms. The duration of the PMD system's fault observation was 282 ms.

The fault log provides the most basic information about the related events. The chronology provides a graphical representation of the appearance of the disturbance and related reactions of the protection relays with their distance protection functions and the reactions of the circuit breakers. The PMD system compares the actual protection relay actions to the event tree analysis and simulation in the fault analysis. Additionally, the protection specialist can provide the final decision on the correctness of operation of the analyzed protection function.

*Figure 5: Event report for a three-phase fault in test no. 1*

The disturbance records collected from both protection relays were synchronized automatically to a common time scale. The time synchronization is presented in the next test. The PMD system also created the fault express report, relay analysis report, and report on comparing the measurements.

4.2   Time synchronization test

The time synchronization was tested separately, where the clocks of both protection relays were not synchronized. Consequently, a large phase shift between the line currents and voltages measured by both relays can be seen in Figure 6. The phase angle difference of U_b in the voltage vectors of both three-phase systems before the time synchronization was found to be 105 °. The PMD system synchronized the measured voltages and currents automatically to a common time scale with very high accuracy. The observed U_b voltage phasors were synchronized with an accuracy of less than 0.1 ° (Figure 6).

5   SUMMARY

The PMD systems are becoming a significant part of modern EPSs because of their ever-increasing size and complexity. Implementing PMD systems can improve the reliability of EPS operations by detecting unwanted changes in the protection relay settings. The discussed PMD system was tested successfully using the hardware in the loop configuration, where the PMD system monitored two numerical distance protection relays connected to the RTDS, which simulated different fault types.

Before time synchronization

After time synchronization
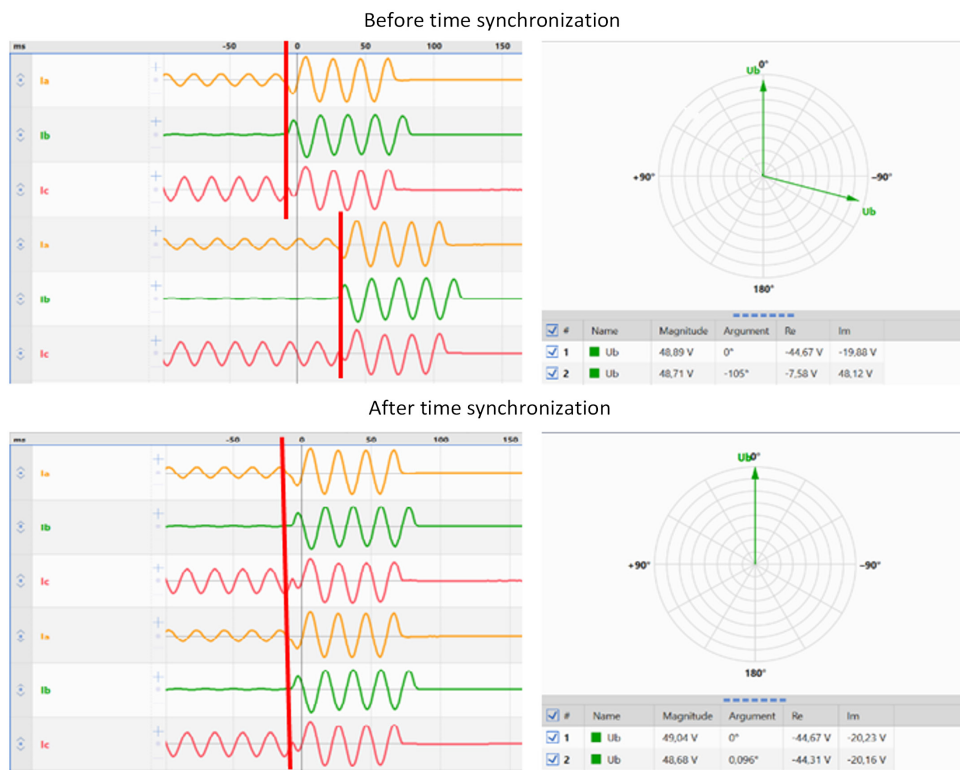
Figure 6: *PMD system time synchronization*

With the hardware in the loop tests, it was confirmed that the PMD system, developed by the Kontron company, is capable of:

1. monitoring the two protection relays and their auxiliary equipment continuously, and detecting different short circuits along with additional events of the restarting relay and voltage transformer fault;

2. verifying the actual protection relay settings periodically, and comparing them with the reference one;

3. detecting and identifying different short circuit types and locating faults on the power line accurately;

4. performing the express analysis of faults based on real-time signals and other data acquired from the protection relays;

5. generating the disturbance report automatically within 2 to 5 minutes after the disturbance occurred;

6. notifying the responsible personnel about the event, whether it was a disturbance or relay malfunction.

Moreover, the discussed PMD system can also be integrated with comprehensive EPS simulation tools, which can be used to deepen the analysis of the protection operations further, including a protection starting evaluation and the correctness of protection settings, but this integration was not tested. Automatic report generation might take more than several minutes in larger EPS and large-scale fault events. However, the same work can take hours, or even days, when done manually. Therefore, using such a PMD system can reduce the workload of protection specialists significantly.

Acknowledgment

References

[1] **V. Salehi, A. Mohamed, A. Mazloomzadeh and O. A. Mohammed**, *Laboratory-Based Smart Power System, Part II: Control, Monitoring, and Protection*, in IEEE Transactions on Smart Grid, vol. 3, no. 3, pp. 1405-1417, Sept. 2012, doi: 10.1109/TSG.2012.2194519

[2] **S. Peyghami, P. Palensky and F. Blaabjerg**, *An Overview on the Reliability of Modern Power Electronic Based Power Systems*, in *IEEE Open Journal of Power Electronics*, vol. 1, pp. 34-50, 2020, doi: 10.1109/OJPEL.2020.2973926

[3] **North American Reliability Corporation (NERC)**: *State of Reliability, An assessment of 2020 Bulk Power System performance,* 2021, *Available:* https://www.nerc.com/pa/RAPA/PA/Performance%20Analysis%20DL/NERC_SOR_2021.pdf

[4] **A. G. Phadke, J. S. Thorp**, *Expose hidden failures to prevent cascading outages [in power systems]*, in IEEE Computer Applications in Power, vol. 9, no. 3, pp. 20-23, July 1996, doi: 10.1109/67.526849

[5] **D. C. Elizondo**, J. de La Ree, A. G. Phadke and S. Horowitz, *Hidden failures in protection systems and their impact on wide-area disturbances*, 2001 IEEE Power Engineering Society Winter Meeting. Conference Proceedings (Cat. No.01CH37194), Columbus, OH, USA, 2001, pp. 710-714 vol.2, doi: 10.1109/PESW.2001.916941

[6] **L. Zhao, X. Li, M. Ni, T. Li and Y. Cheng**, *Review and prospect of hidden failure: protection system and security and stability control system,* in Journal of Modern Power Systems and Clean Energy, vol. 7, no. 6, pp. 1735-1743, November 2019, doi: 10.1007/s40565-015-0128-9

[7] **A. K. Barnes, A. Mate and J. E. Tabarez,** *The Risk of Hidden Failures to the United States Electrical Grid and Potential for Mitigation*, 2021 North American Power Symposium (NAPS), College Station, TX, USA, 2021, pp. 1-6, doi: 10.1109/NAPS52732.2021.9654709

[8]   **A. G. Phadke, P. Wall, L. Ding and V.** Terzija, *Improving the performance of power system protection using wide area monitoring systems*, in Journal of Modern Power Systems and Clean Energy, vol. 4, no. 3, pp. 319-331, July 2016, doi: 10.1007/s40565-016-0211-x

[9]   **V. Terzija, G. ValverdFe, D. Cai, P. Regulski, V. Madani, J. Fitch, S. Skok, M. Begovic, A. Phadke**: *Wide-Area Monitoring, Protection and Control of Future Electric Power Networks,* IEEE, Vol. 99, No. 1, p.p. 80-93, 2011

[10] **J. Wen, W. -H. E. Liu, P. L. Arons and S. K. Pandey**, *Evolution Pathway Towards Wide Area Monitoring and Protection—A Real-World Implementation of Centralized RAS System*, in IEEE Transactions on Smart Grid, vol. 5, no. 3, pp. 1506-1513, May 2014, doi: 10.1109/TSG.2013.2278660

[11] D. Baltensperger, S. Sanchez, S. D'Arco and K. Uhlen, *Assessing Hardware in the Loop Approaches for Wide-Area Monitoring Control and Protection Devices,* in IEEE Transactions on Power Delivery, vol. 38, no. 4, pp. 2724-2734, Aug. 2023, doi: 10.1109/TPWRD.2023.3255414

[12] **P. Gadde, S. Brahma, T. Patel,** *Real-Time Hardware-in-The-Loop Implementation of Protection and Self-Healing of Microgrids*, in IEEE Transactions on Industry Applications, vol. 59, no. 1, pp. 403-411, Jan.-Feb. 2023, doi: 10.1109/TIA.2022.3215624

[13] **J. Westman, R. Hadidi, C. Fox, J. Leonard and A. Harrell**, *Controller Hardware-in-the-Loop Testing of an IEC 61850 GOOSE Based Control for Seamless Transition of a Microgrid Between Island and Grid-Connected Modes*, in IEEE Transactions on Industry Applications, vol. 57, no. 1, pp. 61-69, Jan.-Feb. 2021, doi: 10.1109/TIA.2020.3029021

[14] **A. A. Memon and K. Kauhaniemi**, *Real-Time Hardware-in-the-Loop Testing of IEC 61850 GOOSE-Based Logically Selective Adaptive Protection of AC Microgrid,* in IEEE Access, vol. 9, pp. 154612-154639, 2021, doi: 10.1109/ACCESS.2021.3128370

[15] **J. R. Camarillo-Peñaranda, M. Aredes and G. Ramos**, *Hardware-in-The-Loop Testing of a Distance Protection Relay*, in IEEE Transactions on Industry Applications, vol. 57, no. 3, pp. 2326-2331, May-June 2021, doi: 10.1109/TIA.2021.3066328

[16] **J. Y. R. Wong, C. Tan, A. H. A. Bakar and H. S.** Che, *Selectivity Problem in Adaptive Overcurrent Protection for Microgrid With Inverter-Based Distributed Generators (IBDG): Theoretical Investigation and HIL Verification,* in IEEE Transactions on Power Delivery, vol. 37, no. 4, pp. 3313-3324, Aug. 2022, doi: 10.1109/TPWRD.2021.3126897

[17] **M. Vygoder, M. Milton, J. D. Gudex, R. M. Cuzner and A. Benigni**, *A Hardware-in-the-Loop Platform for DC Protection*, in IEEE Journal of Emerging and Selected Topics in Power Electronics, vol. 9, no. 3, pp. 2605-2619, June 2021, doi: 10.1109/JESTPE.2020.3017769

[18] **D. Liu, Q. Hong, A. Dysko, D. Tzelepis, C. Booth, I. Cowan, B. Ponnalagan**, *Hardware-in-the-loop tests and analysis of hvdc system's impact on distance protection performance,* The 17th International Conference on AC and DC Power Transmission (ACDC 2021), Online Conference, 2021, pp. 96-101, doi: 10.1049/icp.2021.2451

[19]   **K. Shahid, K. Nainar, R. L. Olsen, F. Iov, M. Lyhne, G. Morgante**: *On the Use of Common Information Model for Smart Grid Applications — A Conceptual Approach*, in IEEE Transactions on Smart Grid, vol. 12, no. 6, pp. 5060-5072, Nov. 2021, doi: 10.1109/TSG.2021.3095896

[20]   **Y. Wang, P. Sai**, *Design and Optimization of an Intelligent Monitoring System for Overhead Lines Based on Common Information Model*, in IEEE Access, vol. 12, pp. 31386-31398, 2024, doi: 10.1109/ACCESS.2024.3368702

[21]   **K. Buthelezi, M. Kabeya, M. Leoaneka**, *A Review of Fault Location Algorithms Utilising Travelling Wave, Wavelet Transform and Multi-Resolution Analysis Techniques*, 2022 30th Southern African Universities Power Engineering Conference (SAUPEC), Durban, South Africa, 2022, pp. 1-6, doi: 10.1109/SAUPEC55179.2022.9730632

Nomenclature

(Symbols)	(Symbol meaning)
CT	Current Transformer
EPS	Electric Power System
C-HIL	Controller Hardware-in-the-Loop
PAC	Protection, Automation and Control
PMD	Protection Monitoring and Diagnostic
RTDS	Real Time Digital Simulator
VT	Voltage transformer
C_0	Capacitance of the zero sequence
C_p	Capacitance of the positive (and negative) sequence
L	Total length of the power line
dL	Relative distance from Podlog (side A) to fault location
dL_P	Absolute distance from Podlog to fault location
dL_O	Absolute distance from Obersielach to fault location
R_0	Resistance of zero sequence of the symmetrical components
R_F	Fault resistance
R_{LE}	Resistance value of the distance protection zones for line-earth faults
R_{LL}	Resistance value of the distance protection zones for line-line faults
R_p	Resistance of the positive (and negative) sequence of symmetrical components
X_0	Reactance of the zero sequence

X_p	Reactance of the positive (and negative) sequence
X_{LL}	Reactance of the distance protection zones for line-line and line-earth faults
T_F	Fault duration time
T_{FC}	Total Fault Clearing time
U_b	Voltage of phase "b" in a three-phase system

Journal of Energy Technology

ANALYSIS OF THE CAPACITY OF LiFePO$_4$ BATTERIES BASED ON THE RELEASED ELECTRONS

ANALIZA KAPACITETE LiFePO$_4$ BATERIJ V ODVISNOSTI OD SPROŠČENIH ELEKTRONOV

Matic Krašovic[1] ℞, Peter Virtič[1]

Keywords: redox reaction, battery capacity, cell area, released electrons, charging current

Abstract

The lithium iron phosphate battery, or LiFePO$_4$, has been analysed in this article. Initially, a comprehensive overview was provided concerning the properties and chemistry of batteries. Subsequently, the core focus of the research was addressed, which centred on quantifying the number of electrons released per 1 cm^2 in 1 second in one cell in the battery during charging. Additionally, comparisons were made, to ascertain whether batteries with capacities lower than the one selected for this study impact the number of electrons released during charging, assuming constant battery voltage, cell surface area and current, or whether the number of released electrons remains unaffected by the capacity variations. The analysis was conducted analytically, and demonstrated transparently using the MATLAB software package.

Povzetek

V tem članku je bila analizirana litij-železno-fosfatna baterija oziroma LiFePO4. Na začetku je bil podan celovit pregled lastnosti in kemije baterij. Nato je bilo obravnavano osrednje področje raziskave, ki se je osredotočalo na kvantifikacijo števila elektronov, sproščenih na 1 cm2 v 1 sekundi v 1 celici baterije med polnjenjem. Poleg tega je bila opravljena primerjava, da bi bilo ugotovljeno, ali baterije z manjšimi kapacitetami kot tista, izbrana za to študijo, vplivajo na število

---

℞   Corresponding author: Matic Krašovic, E-mail address: matic.krasovic@student.um.si

[1]   University of Maribor, Faculty of Energy Technology, Krško, Slovenia

sproščenih elektronov med polnjenjem, ob predpostavki konstantne napetosti baterije, površine posamezne celice in toka, ali pa število sproščenih elektronov ostaja nespremenjeno ne glede na variacije kapacitete. Analiza je bila izvedena analitično in bolj pregledno v programskem paketu MATLAB.

1 INTRODUCTION

Nowadays, batteries have become used widely all over the world, and this leads to battery technology developing at a fast-paced rate. Batteries are now key elements in the development of electric vehicles, renewable energy sources, uninterruptible power supplies and portable systems *[1]*.

Lithium batteries are used for energy storage, due to their high-power densities and long lifespan compared to other battery types. Lithium iron phosphate, $LiFePO_4$, delivers good electrochemical performance alongside a low internal resistance of the battery. The $LiFePO_4$ cell is more tolerant to maximal charging conditions, and less stressed than Li-ion based cells when kept under high voltage for long periods. Low temperatures reduce performance, whereas high temperatures shorten the lifespan. $LiFePO_4$ cells have good thermal stability, high abuse tolerance and are safer than Li-ion based chemistries, but also have a higher self-discharging rate *[1]*.

Many things and terminology get mixed up in the field of batteries and their chemistry. That is why this article has been created: to give the readers an overall view of the batteries, cells, terminology such as oxidation, reduction, redox reaction, and, briefly, about the chemistry of the batteries and what is happening inside them, and to make that clear. Furthermore, research has been conducted on the number of electrons released in a chemical reaction. Because this is a redox reaction and the oxidation number of elements changes through the process, many electrons are released through the reaction.

2 LITHIUM IRON PHOSPHATE BATTERY

A battery is a device that converts chemical energy to electrical energy with the help of an electrochemical redox reaction (oxidation-reduction). Since this article talks about the $LiFePO_4$, which can be re-charged, there are two processes that can occur, and these are charging and discharging, so the redox reaction flows in a different way when charging or discharging. A redox reaction includes the flow of electrons from one material to other over the outside electric circuit *[2]*.

2.1 Battery building blocks

A cell is a basic electrochemical unit that converts electrical energy directly from chemical energy. A battery consists of one or more electrochemical cells that are connected electrically in appropriate series or parallel arrangements. A cell is made of four main components *[3]*:

1. An anode, or negative electrode, is an electrode where oxidation is always happening. The anode transmits electrons outside the circuit *[3]*.

2. A cathode, or positive electrode, is an electrode where reduction is always happening. The cathode gathers the electrons which the anode released *[3]*.

3. <u>An electrolyte</u> is an ion conductor, and provides a medium for charge transfer (ions) inside the cell between the anode and cathode. The electrolyte is typically water, or some other form of liquid where different kinds of salts or acids are dissolved *[3]*.

4. <u>A separator</u> is a material that is used for a mechanical separation of the anode and cathode. It is conductive for electrolyte *[3]*.

In this article, the focus will be on the $LiFePO_4$ battery. This type of battery is a secondary battery that can be charged again.

This battery is more tolerant to full charge conditions, and is less stressed than other lithium-ion systems if kept at high voltage for a prolonged time. The cathode is made of lithium iron phosphate ($LiFePO_4$) material, and the anode out of graphitic carbon. Its materials can be seen nicely in the chemical reaction equation, which will be presented further in the article. They are very safe (from damage, shock and fire does not occur spontaneously) *[4]*.

The parameters of the $LiFePO_4$ battery can be seen in Table 1.

Table 1: *Parameters of the $LiFePO_4$ battery [4]*

Lithium iron phosphate	$LiFePO_4$; lithium iron phosphate cathode; graphite anode; short form: LFP
Voltages	12,8 V rated voltage; 3,2 V nominal voltage (one cell); typical operating range: 2,5-3,65V (one cell)
Specific energy	90-120 Wh/kg
Cycle life	2000 and higher (related to the depth of discharge and the temperature)
Thermal runaway	270°C.... very safe battery, even if fully charged
Currents	They vary, and are related to capacitance (Ah)

3   BATTERY OPERATIONS OF AN LiFePO$_4$

3.1   Discharging process of an LiFePO$_4$

When the battery/cell relates to outside load, electrons flow from the negative anode (which is oxidised) over the load on the positive cathode, which collects the electrons (and is reduced). As the battery is used and the reactions at both electrodes chug along, new chemical products are produced *[5]*. The discharging process can be seen in Fig. 1.
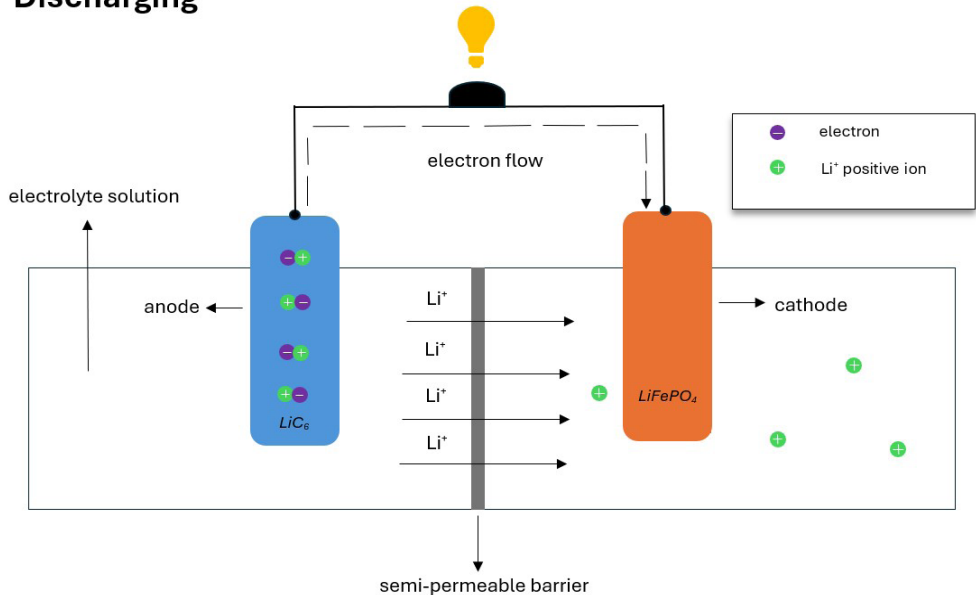
Discharging

Figure 1: LiFePo$_4$ discharging *[own source]*

3.2   Charging process of an LiFePO$_4$

In the charging process the flow of electrons is in the other direction than before. Now, let us clarify some definitions, as it was said in the Abstract. Before, the anode was a negative electrode and the cathode positive. Now, when the process flows in other direction, it can be said that, on the positive electrode, there is an oxidation, and on the negative a reduction. By definition, an anode is an electrode where oxidation happens and a cathode where reduction happens. In this case, a positive electrode is an anode and a negative one is a cathode. However, when charging of the battery occurs, the anode and cathode replace their positions and + and − stay in their positions *[5]. The c*harging process can be seen in Fig. 2.
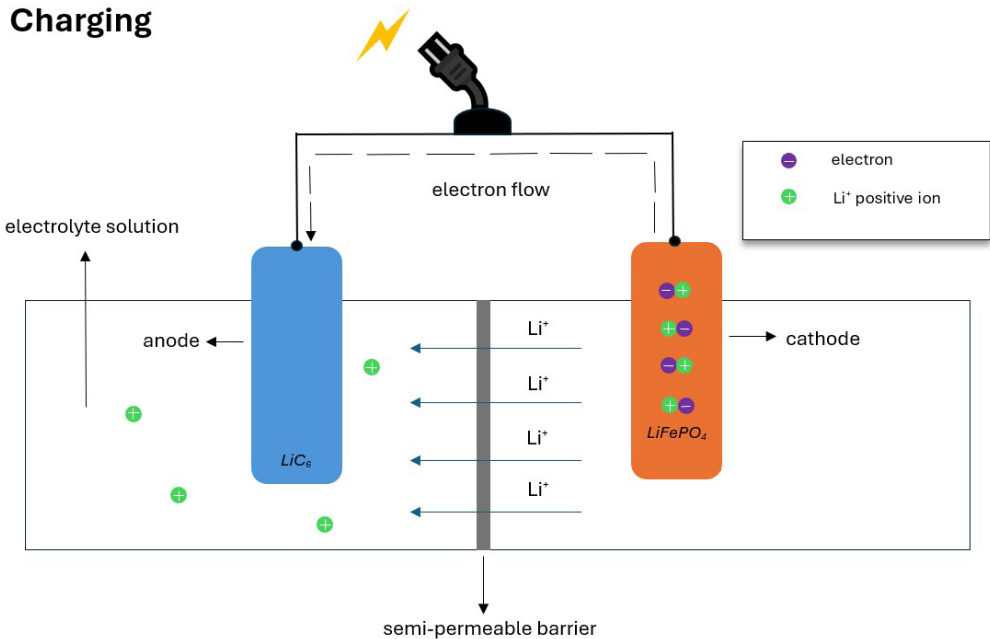
Charging

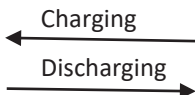**Figure 2:** LiFePo4 charging *[own source]*

3.3 Reactions in discharging and charging of an LiFePO$_4$

The charging and discharging of an LiFePO$_4$ can be shown as an electrochemical reaction which works in both ways *[6]*.

Anode:
$$LiC_6 \leftrightarrow Li^+ + 6C + e^-$$ (3.1)

Cathode:
$$FePO_4 + Li^+ + e^- \leftrightarrow LiFePO_4$$ (3.2)

Charging

⟵

Discharging

⟶

The arrows represent in which way the chemical reaction is happening, due to whether it is discharging or charging.

When the battery is discharging, the anode is negatively charged and the cathode positively, and, when it is charging, the anode is positively charged and the cathode negatively.

4   METHODS OF RESEARCH

An LiFePO$_4$ battery and its chemistry at a more advanced level have been analysed in this article.

A LiFePO$_4$ battery with *Q*=280 Ah and *V*=12,8 V has been taken *[7]*.

This battery is comprised of four cells arranged in a series configuration. Given that the battery's nominal voltage is 12.8 V, the voltage of each individual cell is 3.2 V. Furthermore, with a total capacity of 280 Ah, each cell possesses a capacity of 70 Ah *[7]*.

4.1   Area for calculation

Calculating the surface area is a crucial aspect of this article, as the research seeks to determine the number of electrons released per square centimetre (and per second), assuming that the material is structured such that the chemical reaction occurs solely on the electrode surface. One alternative method will be presented, called the BET method, but I have opted not to pursue it. The decision against this method was made because this method is experimental and requires laboratory execution. Since the calculations are primarily analytical and my focus was not on laboratory work, I chose to compute the surface area using equation (4.5). The method I employed will be detailed after the BET method chapter.

4.1.1   BET method

The BET method is a classic method for the determination of a specific area of some substance, and is carried out around relative pressures between 0,5 and 0,3 bars. In this process, one layer is adsorbed, which helps us determine a specific area by the BET method equation (4.1) *[8]*.

The BET equation can be seen in (4.1):

$$\frac{P_n}{V_a(P_0 - P_n)} = \frac{1}{V_m C} + \frac{C-1}{V_m C} \times \frac{P_n}{P_0}$$

(4.1)

where $\frac{P_n}{P_0}$ is the relative pressure in %, V_a is the adsorbed volume in *cm³,* and V_m is the volume of one layer in *cm³*. C is a constant, which tells the intensity of the reaction between gas and area, and can vary; a higher value means a stronger interaction. *[8]*

The whole area S$_t$ and specific area S are determined by calculating the following two equations (4.2) and (4.3):

$$S_t = \frac{V_m N_A A}{M}$$

(4.2)

$$S = \frac{S_t}{W}$$

(4.3)

where N_A is Avogadro's constant (6,023*20^{23} mol^{-1}), M is a molecule's mass of the gas in *g/mol*, A is a cross-section area of the gas molecule in *cm²* and W is the mass of a substance in *g [8]*.

4.1.2 Proposed method

In this research, the area of the battery has been calculated a little bit differently than the previous alternative – the BET method.

The length of this battery is 533 mm and width 241 mm [7].

That is why the area of one side is calculated as seen in equation (4.4):

$$S = 533mm \times 241mm = 1284{,}53\ cm^2 \tag{4.4}$$

The area of the battery's lower layer has been determined by calculating the equation (4.4). To calculate the area of one cell, equation (4.5) needs to be used:

$$S_c = S \times 0{,}75 \tag{4.5}$$

where S_c is the area of one battery cell and S is the whole area of the battery.

When everything is calculated, the area of one cell equals S_c=963,3975 cm².

The battery's maximum capacitance, denoted as Q', is specified at 280 Ah (ampere-hours). However, capacitance can also be quantified in C (Coulombs), which should not be confused with the C-rate associated commonly with battery charge and discharge rates. Battery capacity is defined as the total amount of electricity generated by the electrochemical reactions in the battery [9].

Given that one Coulomb equates to the flow of one ampere for one second (1C=1A*1s), the conversion of capacitance from ampere-hours to Coulombs can be accomplished using the formula (4.6). This calculation will provide the capacitance in terms of Coulombs, offering an alternative and scientifically equivalent measurement of the battery's storage capacity.

$$Q = Q' \times t = 280Ah \times \frac{3600s}{h} \tag{4.6}$$

where Q is the new capacitance in C, Q' is the old capacitance in Ah and t is the time.

By calculating the new capacitance in equation (4.6), the result equals Q=1008000 C.

The new capacitance is now measured in Coulombs, and this value encompasses the combined capacity of all four cells. However, the research focuses on just a single cell. Therefore, to align the measurements with the study's scope, it was necessary to adjust the starting capacitance, expressed in ampere-hours, to reflect only one cell. The result provides the following equation (4.7):

$$Q'_c = \frac{Q'}{4} = \frac{280Ah}{4} \tag{4.7}$$

where Q'_c is the capacitance of only one cell in Ah.

When Q'_c in equation (4.7) is calculated, the result is $Q'_c = 70$ Ah

We require the capacitance of a single cell to be expressed in the units of ampere-seconds or, equivalently, in Coulombs.

A similar equation as (4.6) has been used in (4.8):

$$Q_c = Q'_c \times t = 70Ah \times \frac{3600s}{h} \qquad (4.8)$$

where Q_c in equation (4.8) is now the capacitance of only one cell in unit C and is equal to Q_c .=252000 C.

After previous calculations of the area of one cell in equation (4.5) and capacitance of one cell in equation (4.8), the results were: S_c=963,3975 cm^2 and Q_c=252000 C.

Everything was prepared to commence the analysis and calculations of the number of released electrons per square centimetre per second in a single cell of an LiFePO$_4$ battery.

To initiate the analysis, it is essential to determine the molar quantity, denoted as n [mol]. According to Faraday's law, the total electric charge Q required to oxidise/reduce the reactant in the redox reaction is proportional to the number of oxidised/reduced substances *[10]*. To do that, the equation (4.9) is needed:

$$Q_c = nFz \qquad (4.9)$$

where n is the molar number in mol, and F is a Faraday constant which equals 96485 C/mol.

In this context, the variable *z* quantifies the number of electrons participating in a single chemical reaction within an exceedingly brief timeframe, which differs from the number of electrons central to the objective of this study. As elucidated in equations (3.1) and (3.2), only a single electron is involved in the reaction mechanism; therefore, for the purposes of analysis, *z* was set to 1.

After a modification of equation (4.9), the new equation (4.10) looks like this:

$$n = \frac{Q_c}{Fz} = \frac{252000 C}{96485 \frac{C}{mol} \times 1} \qquad (4.10)$$

Upon calculating the molar number *n*, the result obtained ws 2,612 mol.

The final step was to calculate what this article has been about, so, electrons released per square centimetre per one second.

Now there are different calculated parameters: S_c=963,3975 cm^2, Q_c=252000 C and n=2,612 mol.

Having determined all the necessary parameters, the calculation of the number of electrons N released can now be proceeded with. Because we know *n*, the equation (4.11) can be used:

$$N = n \times N_A \qquad (4.11)$$

where N represents number of electrons [e$^-$] and N_A is the Avogadro's constant; N_A=6,023*20^{23} particles (e$^-$)/mol.

$$N = 2,612 mol \times (6,023 \times 10^{23} \frac{e^-}{mol}) \qquad (4.12)$$

When *N* is calculated, the result is: $N = 1,573 \cdot 10^{24} e^-$.

The number of electrons released per square centimetre must now be determined, as N in equations (4.12) and (4.13) is calculated over the entire area of one cell. The calculation over one second will be addressed later in the article.

The equations that will determine the result are addressed in (4.13) and (4.14):

$$N_{cm^2} = \frac{N}{S_c} \tag{4.13}$$

$$N_{cm^2} = \frac{1{,}573 \times 10^{24} e^-}{963{,}3975 cm^2} \tag{4.14}$$

For the ith calculation of N over one squared centimetre in equations (4.13) and (4.14) the

result is $N_{cm^2} = 1{,}6328 \cdot 10^{21} \frac{e^-}{cm^2}$.

where N_{cm^2} now represents how many electrons are released in one cell on 1 cm².

It is understood that, for a battery cell with a capacitance of 70 Ah, as specified in this research, the current over a period of one hour would be 70 A, assuming the presence of a resistance that would discharge the battery within this timeframe. However, this definition may vary, as this number is not always exact. In this method, the current will be calculated with the help of its losses through the circuit itself.

The maximum charge rate for a LiFePO$_4$ cell is approximately 26-30 % of the amp-hour rating, as reported in reference [11]. The authors in the cited article [11] provided an example with a lead acid battery, where they utilised 10 % of the amp-hour rating to determine their charging current. For the specific type of battery discussed in this research, the suggested charge rate falls within the range of 26-30 %. Consequently, a median value of 28 % has been adopted for this study.

To calculate the current for a battery with a capacitance of 280 Ah, the following equations (4.15) and (4.16) can be used:

$$I' = Q' \times 0{,}28 \tag{4.15}$$

$$I' = 280 Ah \times 0{,}28 = 78{,}4 \ A \tag{4.16}$$

The discrepancy in units between the left and right sides of the equation (4.16) arises directly from the earlier discussion regarding the percentage of the amp-hour rating, as detailed in reference [11]. After current calculation, this is the result: $I' = 78{,}4 \ A$

In practical terms, it has been observed that losses, while charging, range between 20-40 %, as documented in reference [11]. The authors of article [11] provided an example with a lead acid battery, noting that this type of battery experiences a similar percentage of losses as the battery type discussed in this article. Previously, a median value of amp-hour was selected for the current calculation; similarly, a median value of 30 % will be adopted here, to account for the losses for the charging time calculation.

It can be seen in equation (4.16) that the charging current is 78,4 A.

This allows us to advance to the next stage of the article, which involves determining the charging time, considering the losses.

The calculation for quantifying the losses will be performed in equation (4.17):

$$Q'' = Q' \times 0{,}3 = 280Ah \times 0{,}3 = 84 \; Ah \tag{4.17}$$

$$Q''' = Q' + Q'' = 280Ah + 84Ah = 364 \; Ah \tag{4.18}$$

where Q''' in equation (4.18) is the new capacitance including the original capacitance Q' (280 Ah) of the battery and the battery's losses Q'' (84 Ah).

To proceed with the charging time calculation, equation (4.19) is needed in the most basic form:

$$Q = I \times t \tag{4.19}$$

With rearranging the equation (4.19) and implementing new values inside, the equation (4.20) is needed for the charging time calculation:

$$t = \frac{Q'''}{I_c} = \frac{364Ah}{78{,}4A} = 4{,}64 \; h \tag{4.20}$$

When the calculation from equation (4.20) is done, the charging time equals t=16704 s.

Now that the charging time has been determined using equation (4.20), all the necessary data are available to calculate the main goal of this article

The number of released electrons per square centimetre has been calculated in equation (4.14). The calculation can now be extended to determine also the number of released electrons per second. All that needs to be done is to divide the results from equation (4.14) with the charging time that has been calculated in equation (4.20). The result will provide equation (4.21):

$$N_{cm^2s} = \frac{N_{cm^2}}{t} = \frac{1{,}6328 \times 10^{21} \frac{e^-}{cm^2}}{16704 \; s} \tag{4.21}$$

When the number of electrons from equation (4.21) are calculated, the result is:

$$N_{cm^2s} = 9{,}78 \cdot 10^{16} \frac{e^-}{cm^2 s}.$$

5   RESULTS

It was intended to research how variations in battery capacity impact the number of electrons released in one cell on an area of one square centimetre and within a duration of one second; specifically, whether a decrease in capacity would, correspondingly, result in a reduction in the number of released electrons.

Initially, 4 LiFePO$_4$ battery cells were considered, with 70 Ah capacity. With the data provided, the results concerning the number of electrons released per one square centimetre were obtained, as shown in equation (4.14). Additionally, the number of electrons released per one square centimetre per one second is detailed in equation (4.21). What implications would arise if the capacity were reduced gradually by 1 Ah, down to 25 Ah for a single cell, equivalent to a total of 100 Ah for the entire battery?

The results are shown in Fig. 3.
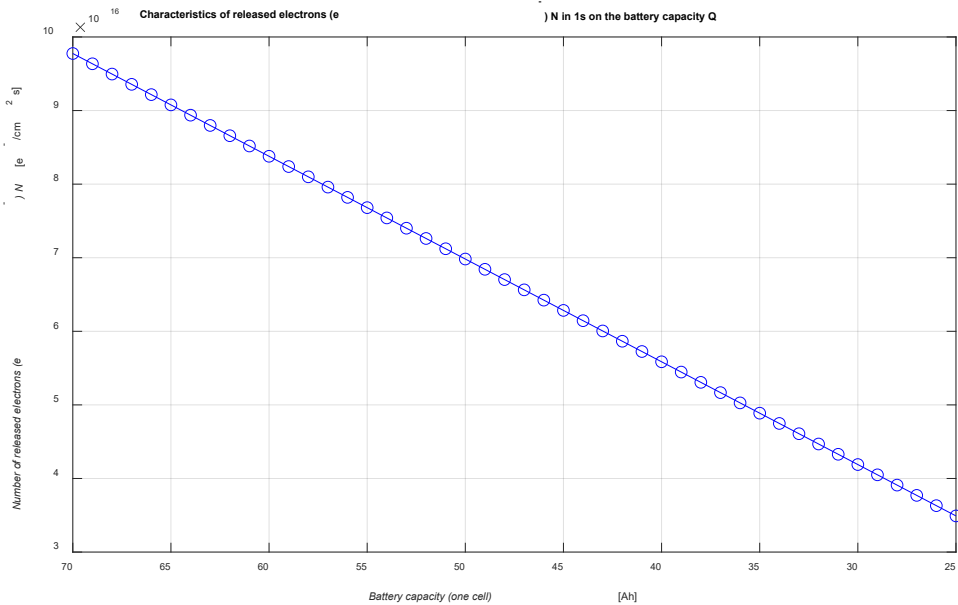
Figure 3: *Characteristics of the released electrons on 1 cm² in 1 s on decreasing battery capacity [own source]*

From Fig. 3 it can be observed that the characteristic is linear. A reduction in the capacity of one cell results in a linear decrease in the number of electrons per one square centimetre per second within a cell. This relationship can also be analysed analytically using the equations that were listed previously. Changes in capacity will affect all other values in the equations, influencing the final outcome, such as the number of electrons. Consequently, an increase in capacity will lead to an increase in the number of electrons, and vice versa.

6   CONCLUSION

The aim of this paper was to determine the quantity of electrons released per square centimetre per second in one of the four cells of an LiFePO$_4$ battery. An analytical approach was adopted, in an effort to determine the quantity of electrons. Calculations were necessary for several parameters, including the surface area of one cell in equation (4.5), the capacitance in Coulombs in equation (4.8), the molar number in equation (4.10) utilising Faraday's constant, and, finally, the number of electrons released per square centimetre per one second in equation (4.21).

The number of electrons was found to be high, which is indicative of a substantial number of chemical reactions occurring, a situation deemed normal for such assessments. It has been calculated in equation (4.16) that the charging current approximates 78,4 A, aligning closely with the theoretical expectations. Specifically, for a single cell with a capacitance of 70 Ah, a charging current of 70 A would be anticipated over one hour given a resistance that discharges the battery in the same timeframe. Nonetheless, the methodology employed in this article diverges slightly, yet the reliability of these results, and others derived through the equations, is affirmed.

Previously, a method to calculate the charging current was introduced, based on taking a percentage of the battery's amp-hour rating. It has been noted that both the losses and the percentage of the amp-hour rating can fluctuate, yet, in this case, and average was utilised, still yielding excellent results.

A decrease in the battery's capacity correlates with a reduction in the number of electrons, thereby producing a smaller charging current. Consequently, such batteries may be more suitable for smaller devices, whereas batteries with a higher initial capacity are better suited for larger devices, due to the greater number of electrons released and the corresponding higher current production. These conclusions were derived analytically through manual calculations, and validated using MATLAB, demonstrating the robustness of the results.

References

[1] **P. Cheng, Y. Zhou, Z. Song and Y. Ou**, "Modelling and SOC estimation of LiFePO4   battery", 2016 IEEE International Conference on Robotics and Biomimetics (ROBIO), Qingdao, China, pp. 2140-2144

[2] **Brooke Schumm**, Britannica, Science & Tech, Battery, https://www.britannica.com/technology/battery-electronics#ref45844 [16.7.2024]

[3] **Battery University,** Battery Building Blocks, https://batteryuniversity.com/article/bu-104b-battery-building-blocks [18.2.2024]

[4] **Battery University**, Types of Lithium-ion, https://batteryuniversity.com/article/bu-205-types-of-lithium-ion, [8.12.2023]

[5] **Australian academy of science**, Technology & the future, How a battery works, https://www.science.org.au/curious/technology-future/batteries [19.3.2024]

[6] **Yin-quan, He-ping, ZHANG Yi, Kai-feng**, Charging Method Research for Lithium Iron Phosphate Battery, SciVerse ScienceDirect, Procedia Engineering Vol. 15 (2011), pp. 4367-4371

[7]   **Amazon**, Eco worthy LiFePO$_4$, 12.8V, 280Ah, https://www.amazon.de/ECO-WORTHY-LiFePO4-Motorhome-Complete-Household/dp/B0CQC41ZTR/ref=sr_1_1_sspa?adgrpid=85748477441&hvadid=394694485907&hvdev=c&hvlocphy=9062551&hvnetw=g&hvqmt=b&hvrand=5943447063617300964&hvtargid=kwd-1440330310&hydadcr=18409_1814169&keywords=lifepo4&qid=1700578740&sr=8-1-spons&sp_csd=d2lkZ2V0TmFtZT1zcF9hdGY&th=1 [29.3.2024]

[8]   **Iztok Dovnik**, Diploma thesis, Preparation and characterization of carvedilol solid dispersions in mesoporous carriers using spray drying method, Ljubljana, 2013

[9]   **Ahmet Aktas, Yagmur Kircicek,** "Solar Hybrid Systems and Energy Storage Systems", "Battery Capacity", Chapter 5, ScienceDirect, 2021, pp. 87-125

[10] **Qi Wang, Qile Wang,** "Electrocatalytic redox neutral [3+2] annulation of N-cyclopropylanilines and alkenes", "Chemical Science", 2021, Vol. 12, pp. 969-975

[11] **ETH CIRCUITS**, Battery charging time & Battery charging current; https://ethcircuits.com/battery-charging-time-battery-charging-current/ [2.1.2024]

Nomenclature

(Symbols)   (Symbol meaning)

t	time
S	Specific area at the BET method
P_n/P_0	Relative pressure
V_a	Adsorbed volume at the BET method
V_m	Volume of one layer at the BET method
C	Constant at the BET method
S_t	Whole area at the BET method
N_A	Avogadro's constant
A	Cross-section area of the gas molecule at the BET method
M	Molecule's mass of the gas at the BET method
W	Mass of the substance at the BET method
S_c	Area of one cell
Q	Capacity in Coulombs of the whole battery
Q'	Capacity in Ah of the whole battery
Q_c'	Capacity in Ah of only 1 cell in the battery
Q_c	Capacity in Coulombs of only 1 cell in the battery

n	molar number
F	Faraday's constant
z	Number of electrons that are used in one chemical reaction
N	Number of released electrons on the whole area of one cell
N_{cm^2}	Number of released electrons on 1 cm^2 in one cell
$N_{cm^2 s}$	Number of released electrons on 1 cm^2 in 1 s in one cell
I'	Charging current through the battery
I_c	Charging current through one battery cell
Q''	Capacitance in terms of losses
Q'''	Starting capacitance + losses

MAIN TITLE OF THE PAPER

SLOVENIAN TITLE

Author[1], Author [2], Corresponding author [℞]

Keywords: (Up to 10 keywords)

Abstract

Abstract should be up to 500 words long, with no pictures, photos, equations, tables, only text.

Povzetek

(Abstract in Slovenian language)

Submission of Manuscripts: All manuscripts must be submitted in English by e-mail to the editorial office at jet@um.si to ensure fast processing. Instructions for authors are also available online at http://www.fe.um.si/en/jet/author-instructions.html.

Preparation of manuscripts: Manuscripts must be typed in English in prescribed journal form (MS Word editor). A MS Word template is available at the Journal Home page.

A title page consists of the main title in the English and Slovenian language; the author(s) name(s) as well as the address, affiliation, E-mail address, telephone and fax numbers of author(s). Corresponding author must be indicated.

Main title: should be centred and written with capital letters (ARIAL bold 18 pt), in first paragraph in English language, in second paragraph in Slovenian language.

Key words: A list of 3 up to 6 key words is essential for indexing purposes. (CALIBRI 10pt)

℞ Corresponding author: Title, Name and Surname, Organisation, Department, Address, Tel.: +XXX x xxx xxx, E-mail address: x.x@xxx.xx

[1] Organisation, Department, Address

[2] Organisation, Department, Address

Abstract: Abstract should be up to 500 words long, with no pictures, photos, equations, tables, - text only.

Povzetek: - Abstract in Slovenian language.

Main text should be structured logically in chapters, sections and sub-sections. Type of letters is Calibri, 10pt, full justified.

Units and abbreviations: Required are SI units. Abbreviations must be given in text when first mentioned.

Proofreading: The proof will be send by e-mail to the corresponding author in MS Word's Track changes function. Corresponding author is required to make their proof corrections with accepting or rejecting the tracked changes in document and answer all open comments of proof reader. The corresponding author is responsible to introduce corrections of data in the paper. The Editors are not responsible for damage or loss of submitted text. Contributors are advised to keep copies of their texts, illustrations and all other materials.

The statements, opinions and data contained in this publication are solely those of the individual authors and not of the publisher and the Editors. Neither the publisher nor the Editors can accept any legal responsibility for errors that could appear during the process.

Chapter examples:

1 MAIN CHAPTER (Arial bold, 12pt, after paragraph 6pt space)

1.1 Section (Arial bold, 11pt, after paragraph 6pt space)

1.1.1 Sub-section (Arial bold, 10pt, after paragraph 6pt space)

Example of Equation (lined 2 cm from left margin, equation number in normal brackets (section.equation number), lined right margin, paragraph space 6pt before in after line):

Equation (1.1)

Tables should have a legend that includes the title of the table at the top of the table. Each table should be cited in the text.

Table legend example:

Table 1: *Name of the table (centred, on top of the table)*

Figures and images should be labelled sequentially numbered (Arabic numbers) and cited in the text – Fig.1 or Figure 1. The legend should be below the image, picture, photo or drawing.

Figure legend example:

Figure 1: *Name of the figure (centred, on bottom of figure, photo, or drawing)*

References

[1]   **N. Surname:** *Title,* Journal Title, Vol., Iss., p.p., Year of Publication

[2]   **N. Surname:** *Title,* Publisher, Year of Publication

[3]   **N. Surname:** *Title* [online], Publisher or Journal Title, Vol., Iss., p.p., Year of Publication. Available: website (date accessed)

Examples:

[1]   **J. Usenik**: *Mathematical model of the power supply system control*, Journal of Energy Technology, Vol. 2, Iss. 3, p.p. 29 – 46, 2009

[2]   **J. J. DiStefano, A.R. Stubberud, I. J. Williams**: *Theory and Problems of Feedback and Control Systems*, McGraw-Hill Book Company, 1987

[3]   **T. Žagar, L. Kegel**: *Preparation of National programme for SF and RW management taking into account the possible future evolution of ERDO* [online], Journal of Energy Technology, Vol. 9, Iss. 1, p.p. 39 – 50, 2016. Available: http://www.fe.um.si/images/jet /Volume 9 Issue1/03-JET_marec_2016-PREPARATION_OF_NATIONAL.pdf (7. 10. 2016)

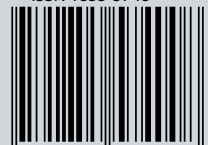Example of reference-1 citation: In text *[1],* text continue.

Nomenclature

(Symbols)	(Symbol meaning)
t	time

JET

9 771855 574008